Mon. Not. R. Astron. Soc. **000**, 1–15 (2014) Printed 22 February 2016 (MN LATEX style file v2.2)

Inferring supernova IIb/Ib/Ic ejecta properties from light curves and spectra: Correlations from radiative-transfer models

Luc Dessart,[1⋆] D. John Hillier,[2] Stan Woosley,[3] Eli Livne,[4] Roni Waldman,[4]

Sung-Chul Yoon,[5] and Norbert Langer.[6]

[1]: *Laboratoire Lagrange, Université Côte d'Azur, Observatoire de la Côte d'Azur, CNRS, Boulevard de l'Observatoire, CS 34229, 06304 Nice cedex 4, France.*
[2]: *Department of Physics and Astronomy & Pittsburgh Particle Physics, Astrophysics, and Cosmology Center (PITT PACC), University of Pittsburgh, 3941 O'Hara Street, Pittsburgh, PA 15260, USA.*
[3]: *Department of Astronomy and Astrophysics, University of California, Santa Cruz, CA 95064, USA.*
[4]: *Racah Institute of Physics, The Hebrew University, Jerusalem 91904, Israel.*
[5]: *Department of Physics and Astronomy, Seoul National University, Gwanak-ro 1, Gwanak-gu, Seoul, 151-742, Republic of Korea*
[6]: *Argelander-Institut für Astronomie, Universität Bonn, Auf dem Hügel 71, 53121, Bonn, Germany*

arXiv:1602.06280v1 [astro-ph.SR] 19 Feb 2016

Accepted . Received

ABSTRACT

We present 1-D non-Local-Thermodynamic-Equilibrium time-dependent radiative-transfer simulations for a large grid of supernovae (SNe) IIb/Ib/Ic that result from the terminal explosion of the mass donor in a close-binary system. Our sample covers ejecta masses $M_{\rm e}$ of 1.7–5.2 $\rm M_\odot$, kinetic energies $E_{\rm kin}$ of 0.6–5.0$\times10^{51}$ erg, and ^{56}Ni masses of 0.05–0.30 $\rm M_\odot$. We find a strong correlation between the ^{56}Ni mass and the photometric properties at maximum, and between the rise time to bolometric maximum and the post-maximum decline rate. We confirm the small scatter in $(V-R)$ at 10 d past R-band maximum. The quantity $V_{\rm m}\equiv\sqrt{2E_{\rm kin}/M_{\rm e}}$ is comparable to the Doppler velocity measured from He I 5875 Å at maximum in SNe IIb/Ib, although some scatter arises from the uncertain level of chemical mixing. The O I 7772 Å line may be used for SNe Ic, but the correspondence deteriorates with higher ejecta mass/energy. We identify a temporal reversal of the Doppler velocity at maximum absorption in the $\sim1.05\,\mu$m feature in all models. The reversal is due to He I alone and could serve as a test for the presence of helium in SNe Ic. Because of variations in composition and ionisation, the ejecta opacity shows substantial variations with both velocity and time. This is in part the origin of the offset between our model light curves and the predictions from the Arnett model.

Key words: radiation hydrodynamics – stars: atmospheres – stars: supernovae - stars: evolution

1 INTRODUCTION

The origin of supernovae (SNe) IIb/Ib/Ic remains somewhat elusive. While the close-binary evolution scenario offers an attractive solution to both core-collapse SN statistics (see, e.g., Podsiadlowski et al. 1992; Eldridge et al. 2008; Smith et al. 2011) and inferred ejecta properties (Ensman & Woosley 1988; Woosley et al. 1995), it is not clear today what fraction arises from the explosion of stars that evolve in isolation. The diversity of massive close binaries can qualitatively explain the observed diversity of SNe IIb (Claeys et al. 2011), but for moderate main-sequence masses, the binary channel seems to favour the production of SNe Ib (Yoon et al. 2010). The distinction between SNe Ib and Ic, which is observational (Wheeler & Levreault 1985; Harkness et al. 1987; Filippenko et al. 1990; Wheeler et al. 1987), is challenged by the presence of broad lines, causing blending/overlap, and the difficulty of exciting He I (Lucy 1991). Non-thermal processes and mixing complicates the interpretation of observations (Dessart et al. 2012). More work is needed to understand these events adequately. In our approach, we try to address these issues by modelling the SN radiation. Our goal is to complement, and also to confront to, the independent inferences based on SN-subtype distribution, host properties (see, e.g., Anderson & James 2008, 2009; Anderson et al. 2010, 2012; Arcavi et al. 2010; Modjaz et al. 2011; Sanders et al. 2012; Kelly & Kirshner 2012; Crowther 2013), or pre-SN star

⋆ email: Luc.Dessart@oca.eu

© 2014 RAS

properties (Yoon et al. 2012; Eldridge et al. 2013; Groh et al. 2013; Kim et al. 2015).

Most simulations of SN IIb/Ib/Ic radiation to date have been limited to grey/multi-frequency radiation hydrodynamics, which delivers bolometric and/or multi-band light curves (see, e.g., Blinnikov et al. 1998; Bersten et al. 2012), and to steady-state radiative transfer (see, e.g., Sauer et al. 2006). In contrast, our method provides the emergent flux as a function of wavelength and time by means of a solution to the time-dependent non-local thermodynamic equilibrium (non-LTE) radiative transfer problem that takes as initial conditions a physical model of the star and its explosion (Dessart & Hillier 2010; Hillier & Dessart 2012) — we give a brief summary of our numerical approach with CMFGEN and on the atomic data used in the calculations in Appendix A. We can thus attempt to directly link SN signatures to the progenitor structure and the explosion properties. By treating the problem in non-LTE, we can include the time-dependent and non-thermal terms that appear in the statistical-equilibrium equations. This is a prerequisite for the description of H and He, and therefore for the understanding of SNe IIb, Ib, and Ic (Dessart et al. 2011, 2012).

Dessart et al. (2015) presented results for three SN ejecta models stemming from the explosion of the mass donor in moderate-mass massive stars evolved in a close-binary system with an initial orbital period of ≈ 4 d (Yoon et al. 2010). These selected SN models were of type IIb, Ib, and Ic and served to investigate the properties of the radiative transfer in these ejecta. Here, we broaden the scope and consider the entire grid of 27 models. The numerical approach is described in Dessart et al. (2015). Numerous properties of these pre-SN models and the corresponding ejecta are provided in tabulated form in the appendix. Our grid comprises models 3p0, 3p65, 4p64, 5p11, and 6p5 (where the name refers to the pre-SN mass of the primary star), which were evolved at a metallicity of 0.02 (models 3p0, 3p65, 5p11, and 6p5) or 0.004 (model 4p64). The main-sequence masses for these systems were 18 $M_\odot \oplus$ 17 $M_\odot$ (model 3p0; $P_{\rm orb,init} = 3$ d), 16 $M_\odot \oplus 14\,M_\odot$ (model 3p65; $P_{\rm orb,init} = 5$ d), 18 $M_\odot \oplus 12\,M_\odot$ (model 4p64; $P_{\rm orb,init} = 5$ d), 60 $M_\odot \oplus 40\,M_\odot$ (model 5p11; $P_{\rm orb,init} = 7$ d), and 25 $M_\odot \oplus$ 24 $M_\odot$ (model 6p5; $P_{\rm orb,init} = 6$ d). Upon reaching iron core collapse, the models were exploded by means of a piston to produce four different asymptotic ejecta kinetic energies $E_{\rm kin}$. We adopt the following nomenclature:

- Suffix C: $E_{\rm kin} = 0.6 \times 10^{51}$ erg. Other models are scaled in energy by a factor of about 2, 4, and 8.
- Suffix A: $E_{\rm kin} = 1.2 \times 10^{51}$ erg. We take this as the standard core-collapse SN ejecta kinetic energy at infinity.
- Suffix B: $E_{\rm kin} = 2.4 \times 10^{51}$ erg.
- Suffix D or G: $E_{\rm kin} = 5.0 \times 10^{51}$ erg. The difference between the two is whether the piston that injects the energy is placed at the edge of the iron core or where the entropy rises to 4 k_B per baryon (which is further out).

The ejecta mass $M_{\rm e}$ for models 3p0, 3p65, 4p64, 5p11, and 6p5 depends on explosion energy (as well as on mixing, but only very slightly) and is 1.71–1.73, 2.18–2.23, 3.11–3.21, 3.54–3.63, and 4.95–5.18 $M_\odot$, respectively. All these simulations leave behind a neutron star, with a mass in the range 1.27–1.57 $M_\odot$ (see Table B1).

Figure 1 shows the distribution of $M(^{56}{\rm Ni})$, "representative" expansion rate $V_{\rm m} \equiv \sqrt{2E_{\rm kin}/M_{\rm e}}$, $E_{\rm kin}$, and pre-SN mass for the full grid of models. The ^{56}Ni mass lies between 0.05 and 0.3 $M_\odot$, although most of our simulations produce $\lesssim 0.1\,M_\odot$. While the kinetic energy is specified by the user as a parameter of the explosion simulation, the ^{56}Ni mass is a byproduct of the explosion, controlled physically by the explosion power and energy as well as the progenitor core structure and composition. For a given progenitor model, the larger the explosion energy, the larger the ^{56}Ni mass. If we consider the full model set, the maximum ^{56}Ni yield tends to increase for larger mass progenitors because they have a larger density above the iron core. Finally, to account for multi-dimensional effects associated with the explosion mechanism (Fryxell et al. 1991b; Wongwathanarat et al. 2015), we enforce two levels of mixing in these models, one moderate (suffix x1) and one strong (suffix x2) — see Dessart et al. (2015) for details.

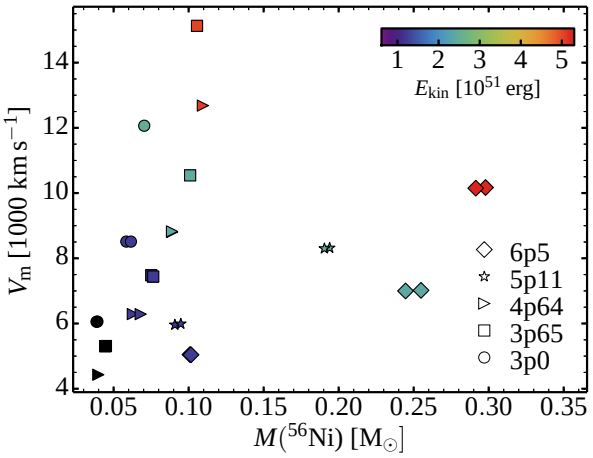

Figure 1. Distribution of $M(^{56}{\rm Ni})$, ejecta kinetic energy $E_{\rm kin}$, and expansion rate $V_{\rm m} \equiv \sqrt{2E_{\rm kin}/M_{\rm e}}$ for our grid of models (pre-SN masses are shown with a different symbol). For a given progenitor, both the expansion rate $V_{\rm m}$ and the ^{56}Ni mass increase with explosion energy.

The SN type associated with each model was discussed in Dessart et al. (2015). Ejecta models 3p0, 3p65, 4p64 contain some residual hydrogen in the outermost parts and helium represents at least 50% of their composition. These models make a type IIb for all explosion energies and mixing values used here. Ejecta model 6p5 is hydrogen deficient and helium represents $\approx 35\%$ of its composition. This model makes a type Ib for all explosion energies and mixing values used here. Because it is hydrogen deficient and poor in helium, ejecta model 5p11 makes a type Ic for all explosion energies and mixing values used here. Here, we do not yet discuss the suitability of these models to match SNe IIb/Ib/Ic observations.

We select this grid of models so that we encompass a range of mass and composition. We adopt four different explosion energies to cover a range around the representative core-collapse SN value of 10^{51} erg. This ignores the probable correlation between explosion energy and progenitor mass/structure — modelling of the neutrino-driven explosion is necessary to produce a more physically consistent ejecta model (see, e.g., Sukhbold et al. 2015). In our model set, lower explosion energies are probably more suitable for the lower mass progenitors; higher explosion energies may not explode by neutrino power alone but may require some other mechanism, perhaps related to core rotation (Ugliano et al. 2012). The correlations we extract from our results obviously reflect the properties for our set of progenitor/explosion models and should therefore be considered as such. In Nature, SNe Ibc may be associated with lower/higher ejecta masses and energies, different levels of mixing, or may stem from binary massive stars that evolved differently from the main sequence (through variations in mass loss rates

or initial rotation, angular momentum transport etc.). The hope with this model sample and extracted trends is to provide a framework to interpret observations.

To complement the previous study of Dessart et al. (2015), we investigate the trends that emerge from our entire grid of models, in particular the correlations arising from variations in ejecta kinetic energy $E_{\rm kin}$, ejecta mass $M_{\rm e}$, ^{56}Ni mass, and progenitor composition. In turn, we discuss our results for the bolometric luminosity light curves (Section 2), the multi-band light curves (Section 3), the colour evolution (Section 4), and some spectral properties (Section 5). We then confront our results to other works, and in particular discuss the shortcomings of the Arnett model for SNe Ib/c (Section 6). Finally, we present our conclusions (Section 7).

2 BOLOMETRIC PROPERTIES

Figure 2 shows the bolometric light curves for models that share a common ejecta kinetic energy of $\approx 1.2\times10^{51}$ erg, but cover a range of ejecta masses from 1.73 to 4.97 $M_\odot$. Over that range, the rise time to maximum increases monotonically from ≈ 23 to ≈ 42 d. The bolometric luminosity at maximum is comparable between models, within the range 1.32–1.65$\times$ 10^{42} erg s^{-1}, and does not vary monotonically with pre-SN mass. The non-monotonic behaviour arises because the different models have different ^{56}Ni masses (the range is from 0.058 to 0.099 $M_\odot$), and because the lower the ejecta mass, the greater the bolometric maximum (all else being the same). Finally, the post-maximum decline decreases steadily as the ejecta mass increases. The bolometric magnitude drop between maximum and 15 d later decreases from 0.72 to 0.22 mag from model 3p0 to 6p5. This brightness decline correlates with the width of the light curve, which appears very symmetric when plotted with respect to the time of maximum (middle panel of Figure 2).

This trend persists to later times, but it then has a different origin. During the photospheric phase, the width of the light curve is controlled by the trapping of radiation energy, which is stored in optical/UV photons. At nebular times, the decline rate is controlled by the trapping of γ-rays from radioactive decay (bottom panel of Figure 2). The opacity affecting low and high energy photons is fundamentally distinct. In particular, the total opacity to low-energy photons is strongly dependent on ionisation, while the γ-ray opacity is primarily sensitive to the total number of electrons.

Figure 3 shows the diversity of light curves for a given pre-SN model exploded with different energies. As the ejecta kinetic energy increases from 0.62 to 1.22, 2.46, and 5.13$\times10^{51}$ erg, the rise time to bolometric maximum decreases from 31.8 to 19.4 d, and the post-maximum decline increases from 0.45 to 0.72 mag. The luminosity at bolometric maximum is larger for models with a higher ejecta kinetic energy, a feature exacerbated by the shorter rise time and the larger ^{56}Ni mass (a factor of about two between models 4p64Cx1 and 4p64Dx2). An increase in ejecta mass or a decrease in ejecta kinetic energy has a comparable impact on the light curve width (Figures 2 and 3).

In most of our models, the early light curve comprises a short post-breakout "plateau" prior to the rise to maximum (see also Dessart et al. 2011). This post-breakout plateau is brighter for larger progenitor radii and explosion energy (see also Bersten et al. 2012). It is shorter for lower mass ejecta (and enhanced ^{56}Ni mixing; Dessart et al. 2012). These various properties are function of the relative contributions of the shock-deposited and decay energies, and how these energy sources are distributed within the ejecta.

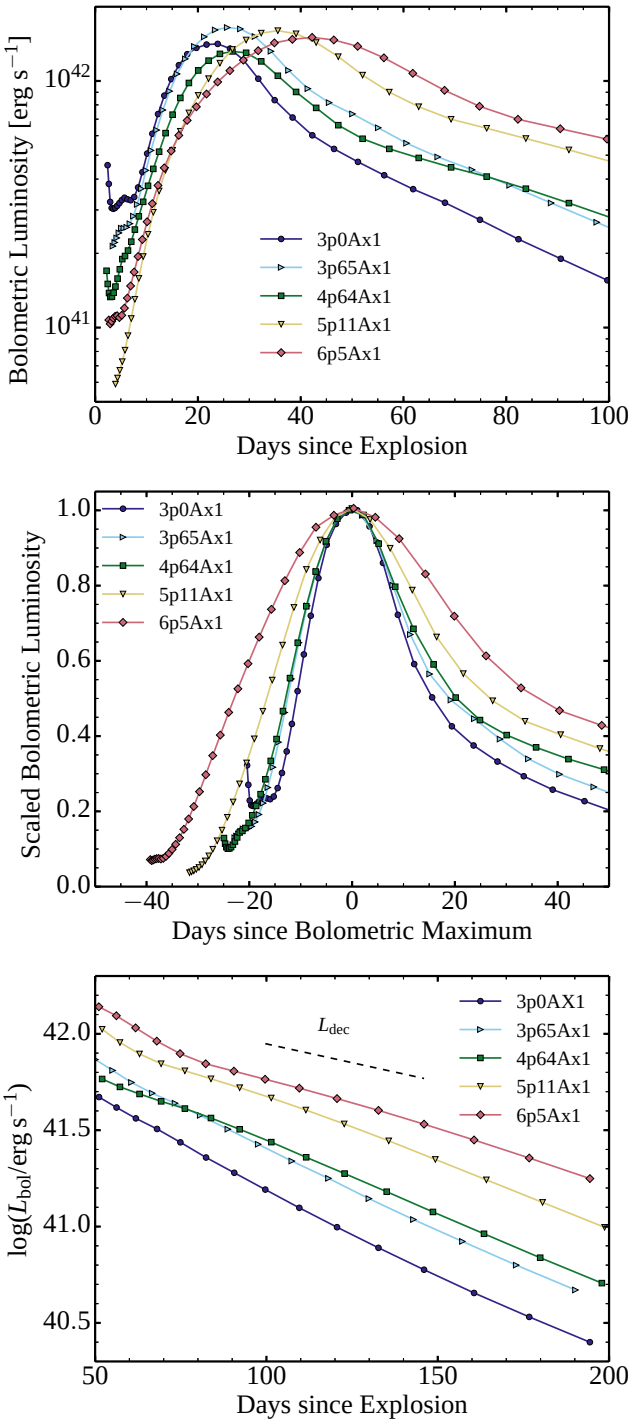

Figure 2. *Top:* Illustration of the bolometric light curves for the models characterised by a 1.2×10^{51} erg explosion energy but covering a range of ejecta masses, from 1.73 (model 3p0Ax1) to 2.23 (model 3p65Ax1), 3.11 (model 4p64Ax1), 3.54 (model 5p11Ax1), and 4.97 $M_\odot$ (model 6p5Ax1). *Middle:* Same as top, but with respect to the time of bolometric maximum and with all light curves normalised to the value at maximum. *Bottom:* Same as top, but with respect to the time of bolometric maximum and limited to the late time evolution. We overlay the power $L_{\rm dec}$ corresponding to the decay of 0.15 $M_\odot$ of ^{56}Ni (dashed line). The larger the mass, the longer the rise to maximum, the smaller the post-maximum brightness decline rate, and the broader the light curve around bolometric maximum.

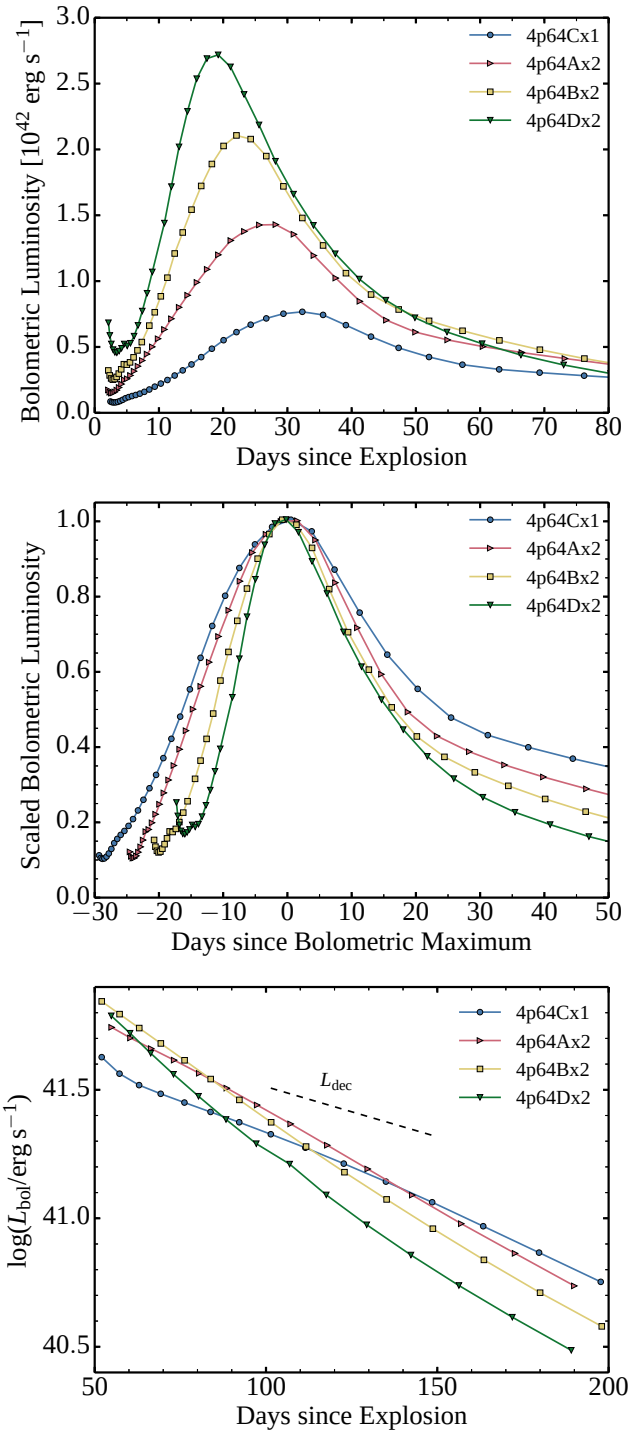

Figure 3. Same as Figure 2, but now for the 4p64 models characterised by different explosion energies (in our nomenclature, $E_{\rm kin}$ grows from 0.6, to 1.2, 2.4, and 5.0×10^{51} erg as we step through models C, A, B, and D). The dashed line (bottom panel) corresponds to the decay power of $0.055\,{\rm M}_\odot$ of ^{56}Ni. Higher explosion energies shorten the rise time to bolometric maximum, increase the post-maximum luminosity decline rate, and produce a narrower light curve around bolometric maximum. In these models, higher explosion energies tend to correlate with the ^{56}Ni mass (Figure 1), which exacerbates the trend seen in the top panel (i.e. higher peak luminosity for higher ejecta kinetic energy).

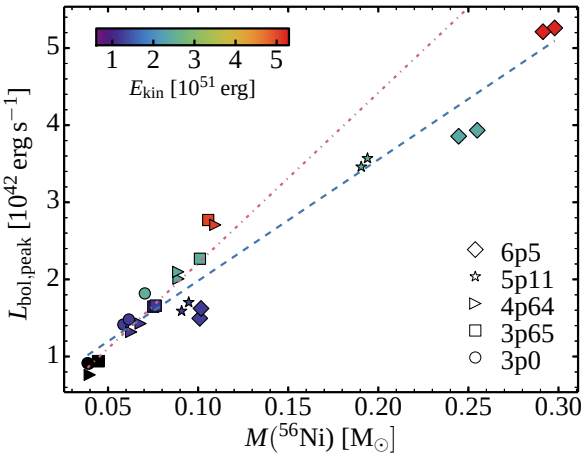

Figure 4. Maximum bolometric luminosity versus ^{56}Ni mass for our grid of models. Symbols correspond to different pre-SN progenitor mass. The colour coding refers to the model kinetic energy. The dashed line corresponds to $L_{\rm bol,peak}/10^{42}\,{\rm erg\,s^{-1}} = 15.718(M(^{56}{\rm Ni})/{\rm M}_\odot) + 0.41$. The dash-dotted curve is the $L_{\rm bol,peak}$ versus $M(^{56}{\rm Ni})/{\rm M}_\odot$ relation for the SN Ia models of Blondin et al. (2013) — the minimum ^{56}Ni mass for that SN Ia model set is actually $0.18\,{\rm M}_\odot$.

Figure 4 shows the distribution of the luminosity at bolometric maximum versus ^{56}Ni for the entire grid of models. This figure shows that ^{56}Ni is, as expected, the key power source behind these SN models. For example, the doubling of the ^{56}Ni mass leads to roughly the doubling of the peak luminosity. However, there is some scatter, which arises from the relatively large range of ejecta masses. For a given ^{56}Ni mass and ejecta kinetic energy, the larger mass ejecta appear under-luminous at maximum because they radiate essentially the same total decay energy but over a longer time. A least-square polynomial fit to the distribution of N model points gives

$$L_{\rm bol,peak}/10^{42}\,{\rm erg\,s^{-1}} = 15.718(M(^{56}{\rm Ni})/{\rm M}_\odot) + 0.41\,.$$

We approximate the dispersion by the quantity $\sqrt{\left[\sum_i (Y_{i,\rm model} - Y_{i,\rm fit})^2\right]/(N-2)}$, where i runs from 1 to N and Y_i is $L_{\rm bol,peak}$ for model i. Here, this dispersion is 0.30×10^{42} erg s^{-1}. This relation is significantly flatter than for SNe Ia (see, e.g., Blondin et al. 2013), probably because of the larger range of ejecta masses for our SNe IIb/Ib/Ic models.

3 PHOTOMETRIC PROPERTIES

The photometric properties discussed in Dessart et al. (2015) are supported by the larger grid of models and so not all properties will be discussed again. We focus on the properties of the R band, which we find to be analogous to that of the bolometric luminosity (Tables C1-C3).

Figure 5 shows the whole set of R-band light curves around maximum. The origin of the x axis is the time of R-band maximum. This reduces the strong overlap caused by the wide range in rise time. It also better reveals the scatter in light curve peaks and widths. One notable difference with the bolometric light curves is the lack of an obvious post-breakout plateau in the R band.

As for the bolometric luminosity, the maximum R-band magnitude correlates with the ^{56}Ni mass. The correlation is strong at

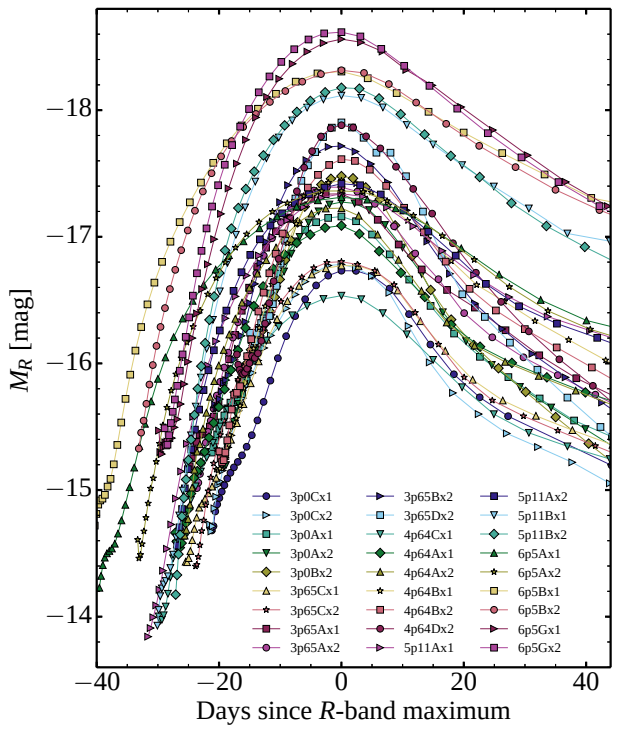

Figure 5. R-band light curves with respect to the time of R-band maximum for the full set of models.

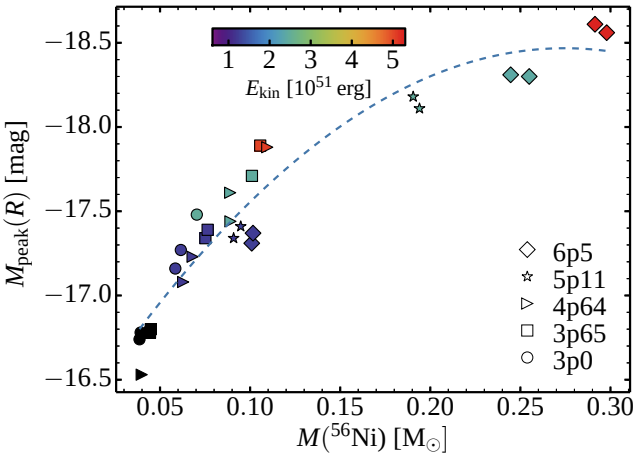

Figure 6. Peak R-band magnitude versus ^{56}Ni mass for our grid of models. The dashed line corresponds to $(M_{\rm peak}(R)/{\rm mag}) = -16.21 - 16.44\,M(^{56}{\rm Ni})/{\rm M}_\odot) + 29.93(M(^{56}{\rm Ni})/{\rm M}_\odot)^2$

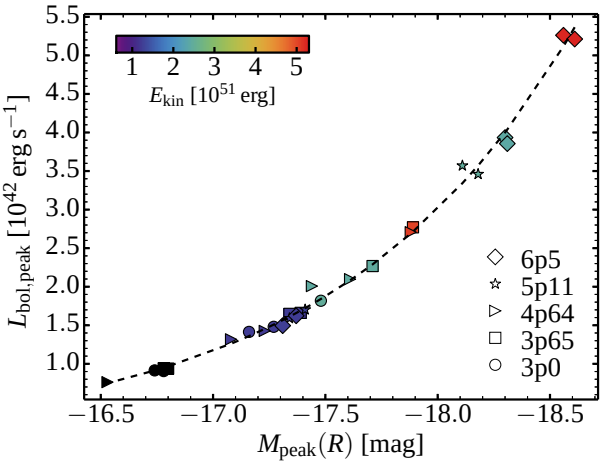

Figure 7. Maximum bolometric luminosity versus maximum R-band magnitude for our grid of models. The dashed curve corresponds to $\log(L_{\rm bol,peak}/10^{42}\,{\rm erg\,s^{-1}}) = -0.41(M_{\rm peak}(R)/{\rm mag}) - 6.92$.

low ^{56}Ni mass and flattens out at large ^{56}Ni mass (Figure 6). A least-square polynomial fit that gives a rough match to the distribution of model results is

$$\frac{M_{\rm peak}(R)}{\rm mag} = -16.21 - 16.44\,\frac{M(^{56}{\rm Ni})}{\rm M_\odot} + 29.93\Big(\frac{M(^{56}{\rm Ni})}{\rm M_\odot}\Big)^2 ,$$

with a dispersion of 0.16 mag. At large ^{56}Ni mass, the fitted curve starts declining, which is unphysical, so this and other fitted formula ought to be used with circumspection. Since the R-band magnitude can be more easily inferred from observations than the bolometric luminosity, we also show how the two compare in Figure 7. The relation that closely holds between the two is

$$\log(L_{\rm bol,peak}/10^{42}\,{\rm erg\,s^{-1}}) = -0.41(M_{\rm peak}(R)/{\rm mag}) - 6.92\,,$$

with a dispersion of 0.017 (in the log) — corresponding to a dispersion of 3-4% in $L_{\rm bol,peak}$.

Figure 8 shows that there is a very strong correlation between the post-maximum decline rate $\Delta M_{15}(R)$ and the rise time $t_{\rm rise}(R)$ to R-band maximum. Using a least-square polynomial fit, our results follow closely the relation

$$t_{\rm rise}/{\rm d} = 57.08 - 71.17\Delta M_{15}(R) + 32.98\Delta M_{15}^2(R)\,,$$

with a dispersion of 2.36 d. This relation holds across a wide range of ^{56}Ni mass, ejecta masses, and ejecta kinetic energies. It simply reflects the fact that the brightening rate to maximum is comparable to the early decline rate after maximum, a property that is expected in the diffusion regime controlling the light curve. This relation may help constrain the explosion time of observed SNe IIb/Ib/Ic, especially those lacking early time observations.

The distribution of $\Delta M_{15}(R)$ and $M_{\rm peak}(R)$ values shows a large scatter (Figure 9) — the same holds if we compare to $M_{\rm peak}(V)$ or $M_{\rm peak}({\rm bol})$. The peak magnitude is primarily controlled by the ^{56}Ni mass, while the post-maximum decline is sensitive to $E_{\rm kin}$, $M_{\rm e}$, as well as ^{56}Ni mass. An example of this complicated sensitivity is that the decay energy tends to raise, or at least maintain, the ionisation and therefore influences the ejecta optical depth. This matters throughout the photospheric phase, which lasts for up to about 2–3 weeks after maximum.

4 COLOUR PROPERTIES

Photometric variations can arise from colour changes. These changes are, however, quite modest in our simulations because the emergent radiation falls primarily within the optical range (Dessart et al. 2015). The pre-SN radius of our models is below $\sim 10\,{\rm R}_\odot$, which causes a significant cooling when the ejecta expands to a SN-like radius in the first week after explosion. Consequently, none of our models appear blue early on. Instead, they show relatively red colours throughout their evolution, with only

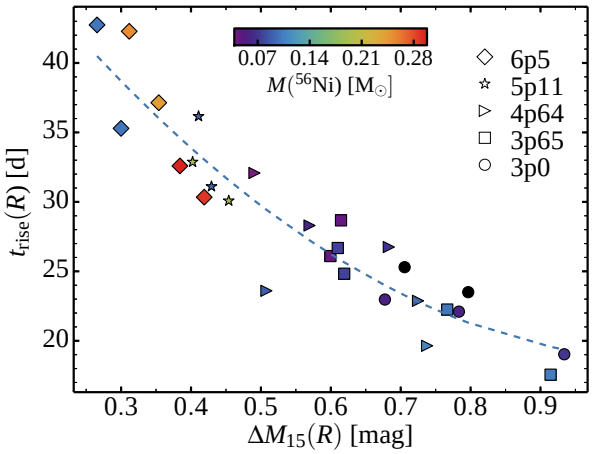

Figure 8. Rise time to bolometric maximum versus post-maximum decline rate $\Delta M_{15}(R)$. for our grid of models. The dashed curve corresponds to $t_{\rm rise}/{\rm d} = 57.08 - 71.17\Delta M_{15}(R) + 32.98\Delta M_{15}^2(R)$

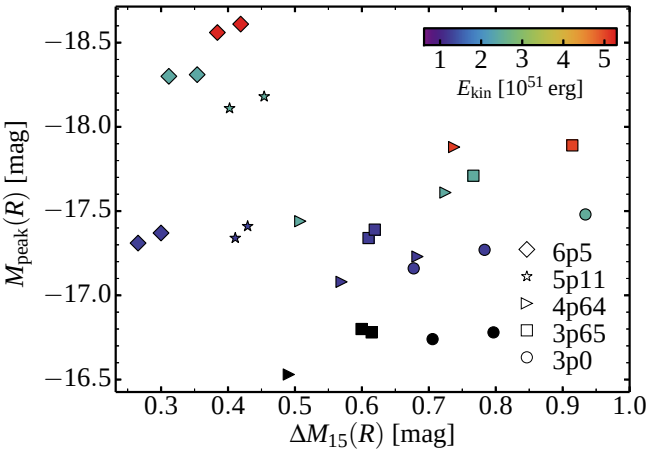

Figure 9. Distribution of R-band peak magnitude versus post-maximum decline $\Delta M_{15}(R)$. The large scatter stems from the complicated dependence of $\Delta M_{15}(R)$ on $E_{\rm kin}$, $M_{\rm e}$ and ^{56}Ni mass.

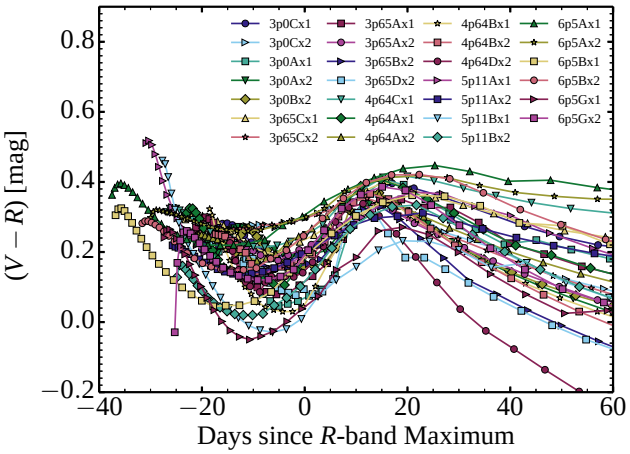

Figure 10. $V - R$ colour light curve with respect to R-band maximum for the full set of models.

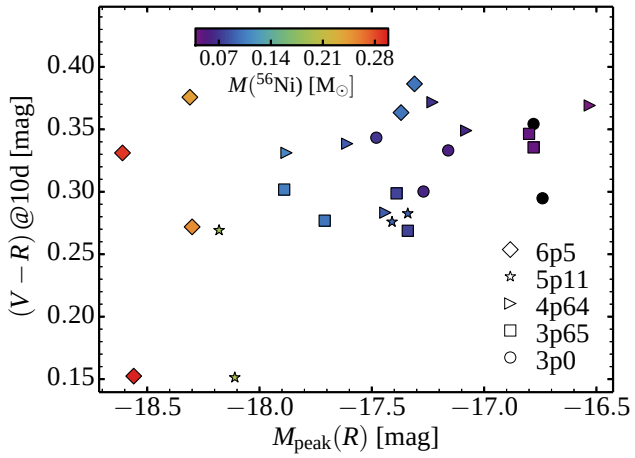

Figure 11. Plot emphasises the degeneracy of $(V - R)$ colour at 10 d after R-band maximum — exceptions to the trend are the high mass high explosion energy moderately-mixed models 6p5Gx1 and 5p11Bx1.

modest variations through the early post-breakout plateau, the rise to maximum, and the post-maximum phase.

Figure 10 shows the evolution of the $(V - R)$ light curve for the whole set of models. There is a first phase of reddening prior to ^{56}Ni decay heating in the spectrum formation region, followed by a hardening on the rise to maximum when ^{56}Ni decay heating is strong, followed by a reddening phase as heating ebbs and line blanketing from metals strengthens.

The $(V - R)$ light curve shows a narrow range of values at 10 d after R-band maximum (Figure 11). This property was identified in observations by Drout et al. (2011) (see also Bianco et al. 2014). In our models, the spectrum forms in the inner ejecta at this epoch. It is influenced by a comparable decay-heating rate, and the composition is similar in all models, with a dominance of C and O at the electron-scattering photosphere at that time. This uniformity of photospheric properties between models is likely responsible for the degeneracy in the $(V - R)$ colour early after peak.

There are two outliers with a bluer colour than the rest of the sample. These models correspond to higher-mass higher-energy ejecta with a high ^{56}Ni mass and characterised by a weaker mixing. Weaker mixing favours higher temperatures in the inner ejecta, causing redder colours early on, but bluer colours around maximum (as discussed in Dessart et al. (2012), weaker mixing has numerous other implications, visible in the bolometric light curve, in the multi-band light curves, and in the spectra). For the full grid of models, the $(V - R)$ colour at 10 d after R-band maximum has a mean value of 0.319 mag and a standard deviation of 0.053 mag. Taking out the two outliers from the set, the mean $(V - R)$ colour value is 0.33 mag and the standard deviation is 0.035 mag.

5 SPECTRAL PROPERTIES

With about 30 model sequences, each containing about 50 time steps, we have a total of 1500 individual spectra. The amount of information contained in such a set of spectra is very large. The salient signatures for models of type IIb, Ib, and Ic were discussed

in Dessart et al. (2015). In this section, we discuss a few important results that emerge from the whole set.

5.1 Hα

In our SN IIb models (3p0, 3p65, and 4p64), Hα is present as a strong line at early times. Its strength decreases with time, such that by the time of maximum, the line may only be visible as a weak absorption. The top panel of Figure 12 shows the evolution of the Doppler velocity at maximum absorption in Hα for our SNe IIb models. In some high-energy explosion models, we lose track of the feature after 1-2 weeks, but in most cases, we can follow $V_{\rm abs}$(Hα) from early times when it is very large, until light curve maximum when its evolution tends to flatten. This asymptotic velocity, which is a factor of ≈ 2 smaller than the initial values, falls in the range 8000-15000 km s^{-1}, and corresponds to the velocity at the base of the shell that contains hydrogen — a smaller asymptotic velocity suggests a larger mass for the H-rich shell (bottom panel of Figure 12 and Tables B1– B2). Lower values are not possible since the deeper layers are hydrogen deficient. In SNe IIb, one can therefore search for that stationary notch to locate the minimum velocity of the hydrogen-rich shell in the ejecta. Interestingly, this property of SN IIb spectra is the only unambiguous, and therefore robust, signature of chemical stratification in SNe IIb/Ib/Ic. It is also observed (Liu et al. 2015).

5.2 He I lines

Figure 13 shows the evolution of the Doppler velocity at maximum absorption in He I 5875 Å, noted $V_{\rm abs}$(He I 5875 Å), for the SNe IIb/Ib in our model set. Qualitatively, the evolution is similar to that of Hα, but shifted to lower values. This arises from the fact that in the corresponding ejecta models, helium is more abundant at depth, where the density is larger, so the maximum line optical depth is reached at lower velocity.

Just like for Hα, the values for $V_{\rm abs}$(He I 5875 Å) tend to level out near maximum. In lower mass ejecta with weaker mixing, there is even a reversal and $V_{\rm abs}$(He I 5875 Å) starts increasing again (the line broadens) after R-band maximum. This effect is more strongly present in the He I 1.083 μm line, although for strong mixing, the reversal is reduced and may even vanish (Figure 14). Observationally, the reversal in $V_{\rm abs}$(He I 5875 Å) is generally not seen in SNe IIb/Ib Liu et al. (2015) — an exception is SN 2011dh (Ergon et al. 2014).

As discussed in Dessart et al. (2015), this flattening and subsequent reversal is a natural consequence of the sensitivity of He I lines to non-thermal processes. Around maximum, as the γ-ray mean free path becomes comparable to the SN radius (see, e.g., figures 1–2 of Dessart et al. 2012), the absorption of γ-rays in the outer ejecta is enhanced. The outer ejecta layers thus become increasingly influenced by non-thermal effects. In general, the outer layers will tend to be more helium rich in SNe IIb/Ib/Ic ejecta, because these correspond to the outer edge of the helium core. Consequently, around R-band maximum, while the bulk of the spectrum forms in the CO-rich regions at the base of the ejecta, the He I 1.083 μm line may start to strengthen and broaden again.

This feature is potentially important. Other species like C, O, Ca are less dependent on non-thermal processes to be excited and to produce lines. They are also more abundant at depth. In contrast, helium is both very sensitive to non-thermal processes and more abundant in the outer ejecta. So, only helium can cause a broadening of the absorption feature seen at $\sim 1.05\,\mu$m in SNe IIb/Ib/Ic spectra. In our models, this broadening is seen even in SN Ic models (i.e., models 5p11Ax1, 5p11Ax2, 5p11Bx1, and 5p11Bx2) and it therefore provides unambiguous evidence for the presence of helium in the model. The behaviour of $V_{\rm abs}$(He I 1.083 μm) could therefore be used to assess the presence of helium in SN Ic ejecta.

High quality near-IR spectra of SNe IIb/Ib/Ic are lacking so a dedicated program to seek such observations is necessary.

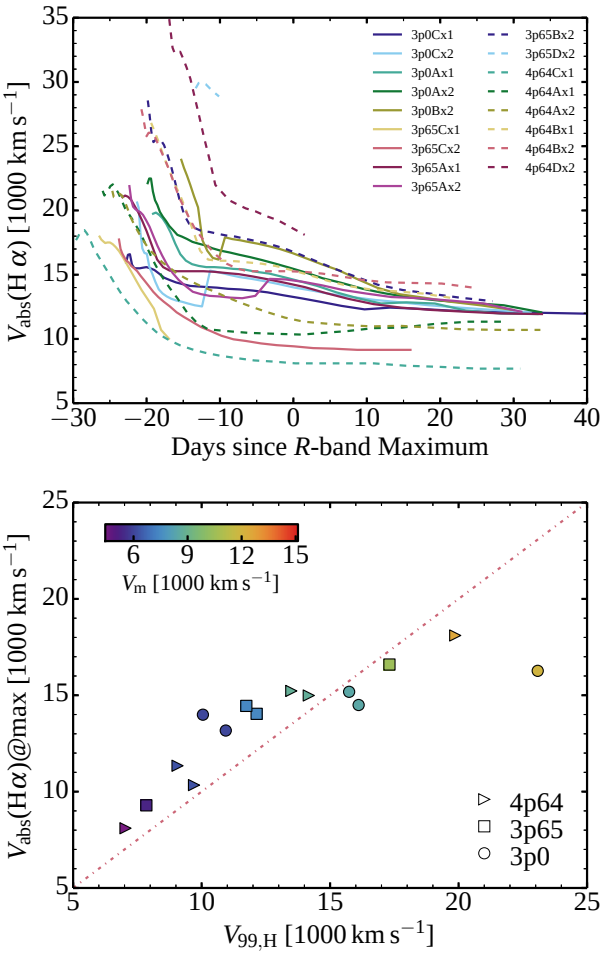

Figure 12. *Top:* Evolution of the Doppler velocity associated with the maximum absorption in Hα, noted $V_{\rm abs}$(Hα), for the SNe IIb models in our sample. *Bottom:* Comparison of $V_{\rm abs}$(Hα) at R-band maximum versus the inner velocity of the shell that contains 99% of the total hydrogen mass, noted V_{99}(H) (integration done inwards from the outermost ejecta location). If both quantities were equal, they would lie along the dash-dotted line.

5.3 Estimate of the ejecta expansion rate

In Dessart et al. (2015), we discussed the ambiguity that surrounds the notion of a photosphere in SNe IIb/Ib/Ic. A more meaningful quantity to constrain is the expansion rate $V_{\rm m} \equiv \sqrt{2E_{\rm kin}/M_{\rm e}}$ since it relates to fundamental quantities characterising a SN ejecta, and it is also used in simplified light-curve modelling. The question is then what line measurement constrains $V_{\rm m}$ with reasonable accuracy?

Figure 15 compares the Doppler velocity at maximum absorption in the line He I 5875 Å at R-band maximum to the expansion rate $V_{\rm m}$ for our set of SNe IIb/Ib models. A least-square polynomial

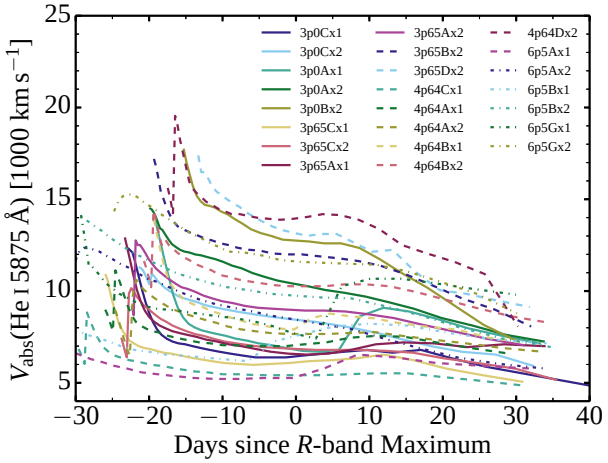

Figure 13. Evolution of the Doppler velocity associated with the maximum absorption in He I 5875 Å for the SNe IIb and Ib models in our sample.

fit to the distribution of points yields

$$\frac{V_{\rm abs}({\rm He\,I\,5875\,\AA})}{1000\,{\rm km\,s^{-1}}} = 2.64 + 0.765\frac{V_{\rm m}}{1000\,{\rm km\,s^{-1}}}\,,$$

with a dispersion of 1370 km s^{-1}. The two quantities are not equal (if so, they would lie on the dash-dotted curve), but they are close. Some of the scatter stems from the different magnitude of mixing between models with suffix x1 and x2. Stronger mixing systematically produces broader He I lines. Unfortunately, we do not know the mixing process with much certainty so reducing the scatter is non trivial. This sensitivity introduces an uncertainty for the estimate of the expansion rate in SNe IIb/Ib, and therefore for the determination of $E_{\rm kin}$ and $M_{\rm e}$.

Figure 16 compares the Doppler velocity at maximum absorption in the line O I 7772 Å at *R*-band maximum to $V_{\rm m}$ for our entire set of models. A least-square polynomial fit to the distribution of points yields

$$\frac{V_{\rm abs}({\rm O\,I\,7772\,\AA})}{1000\,{\rm km\,s^{-1}}} = 2.99 + 0.443\frac{V_{\rm m}}{1000\,{\rm km\,s^{-1}}}\,,$$

with a dispersion of 780 km s^{-1}. The slope is much flatter, i.e., $V_{\rm abs}$(O I 7772 Å) tends to be lower than $V_{\rm m}$, and the offset is greater for increasing ejecta mass and kinetic energy. This probably arises because the oxygen abundance increases inwards in the ejecta, biasing the line optical depth to lower velocities. Also, for higher mass, the peak is delayed so at maximum, the outer ejecta is cold, optically thin, and contributes little to the emergent spectrum. At higher explosion energy, the same result obtains but because the outer ejecta expands faster. Still, for model 5p11, $V_{\rm abs}$(O I 7772 Å) offers a satisfactory means to constrain $V_{\rm m}$ to within 10-20%.

So, we suggest to constrain the expansion rate $V_{\rm m}$ with He I 5875 Å in SNe IIb/Ib and with O I 7772 Å in SNe Ic.

6 COMPARISON TO OTHER WORK

In this section, we compare some results with those estimated using different approaches. In particular, we discuss how our grid of models compares with the energy constraint set by the time-integrated form of the first law of thermodynamics (Section 6.1). We then

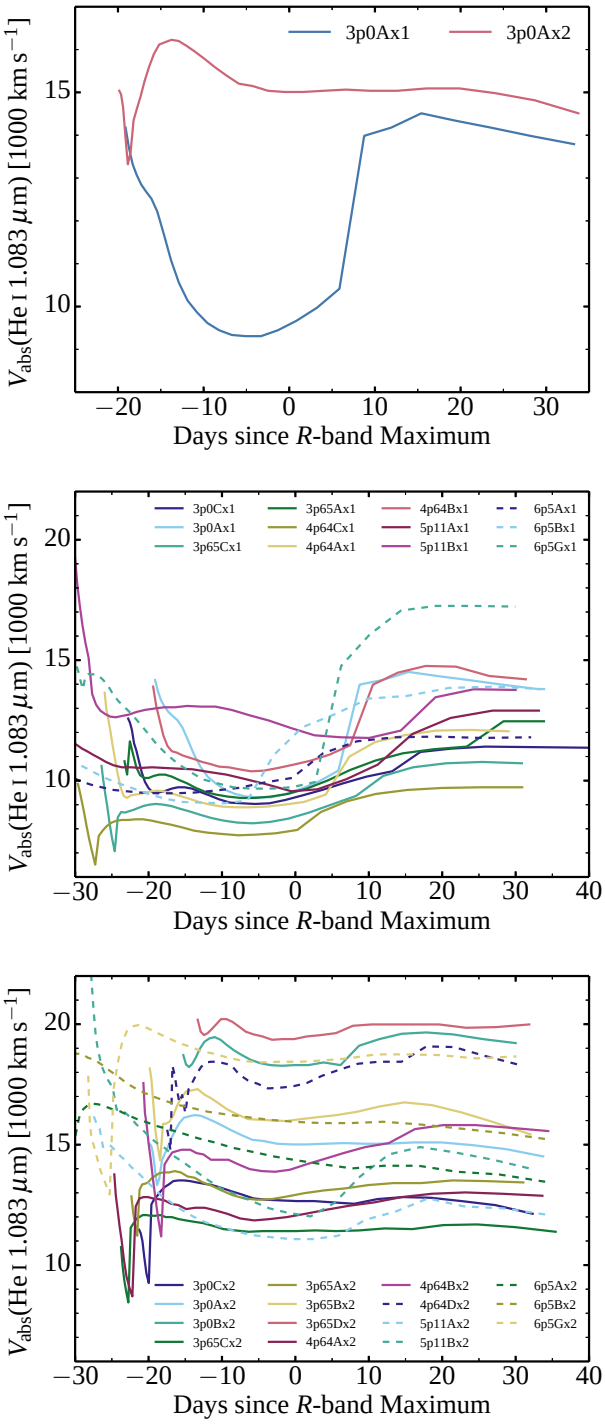

Figure 14. *Top:* Evolution of the Doppler velocity associated with the maximum absorption in He I 1.083 μm for models 3p0Ax1 and 3p0Ax2. *Middle:* Same as top, but now for all models with moderate mixing (x1). *Bottom:* Same as top, but now for all models with strong mixing (x2). In models with moderate mixing, the velocity at maximum absorption decreases near the time of bolometric maximum and increases after maximum due to non-local energy deposition and non-thermal effects. In models with strong mixing, this reversal is weaker, or even absent (e.g., in a low-mass ejecta model like 3p0Ax2). The hook at early times corresponds to the epoch when we switch on non-thermal processes in the CMFGEN calculation.

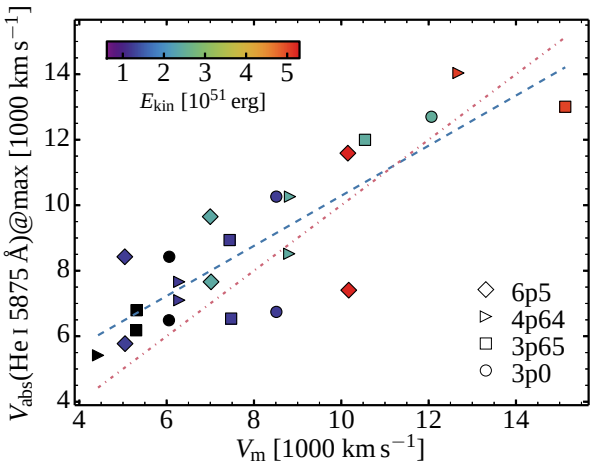

Figure 15. Doppler velocity at maximum absorption in the line He I 5875 Å at R-band maximum versus the quantity $V_{\rm m} \equiv \sqrt{2E_{\rm kin}/M_{\rm e}}$ for our SNe IIb/Ib models (when two identical symbols lie at the same $V_{\rm m}$, the upper symbol corresponds to the model with stronger mixing). The dashed curve is a fit to the distribution of values and has the form $V_{\rm abs}$(He I 5875 Å)/1000 km s^{-1} = 2.64 + 0.765$V_{\rm m}$/1000 km s^{-1}. All values would lie along the dash-dotted curve if the two quantities plotted were equal (i.e., $V_{\rm abs} = V_{\rm m}$).

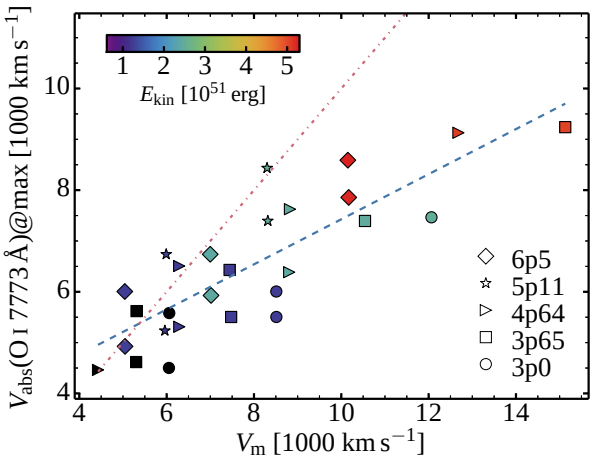

Figure 16. Doppler velocity at maximum absorption in the line O I 7772 Å at R-band maximum versus the quantity $V_{\rm m} \equiv \sqrt{2E_{\rm kin}/M_{\rm e}}$ for our grid of models. (when two identical symbols lie at the same $V_{\rm m}$, the upper symbol corresponds to the model with stronger mixing). The dashed curve is a fit to the distribution of values and has the form $V_{\rm abs}$(O I 7772 Å)/1000 km s^{-1} = 2.99 + 0.443$V_{\rm m}$/1000 km s^{-1}. All values would lie along the dash-dotted curve if the two quantities plotted were equal (i.e., $V_{\rm abs} = V_{\rm m}$).

compare our results to the Arnett model (Arnett 1982), including the so-called Arnett rule (Section 6.2).

6.1 Constraints from energy conservation

Katz et al. (2013) propose to use the energy equation to constrain the ^{56}Ni mass. But we can also use it to gain insights into the physics of SN IIb/Ib/Ic radiation, for example, to check the long-term energy conservation of the CMFGEN sequence.

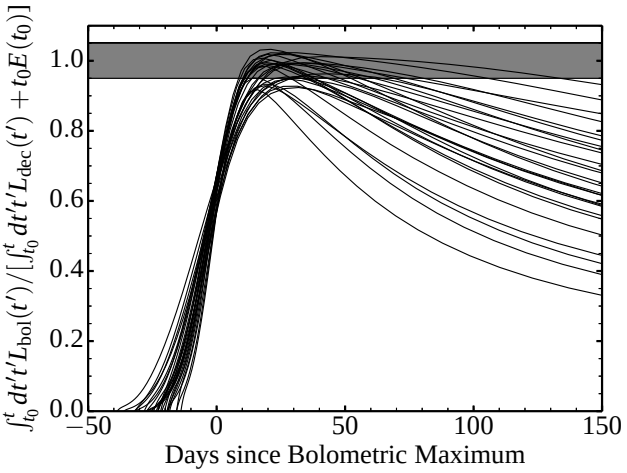

Figure 17. Illustration of the variation of the ratio $\int_{t_0}^{t} dt' t' L_{\rm bol}(t')$ /$[\int_{t_0}^{t} dt' t' L_{\rm dec}(t') + t_0 E(t_0)]$ versus time since bolometric maximum (we use $t_0 \gtrsim 3$ d) for our grid of SNe IIb/Ib/Ic models. The shaded area corresponds to offsets of ±5% from unity. For some models, the ratio remains below unity because of the early escape of γ-rays.

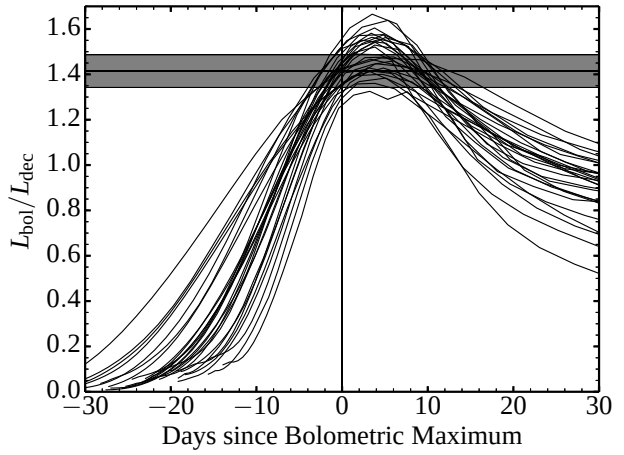

Figure 18. Variation of the ratio $L_{\rm bol}/L_{\rm dec}$ versus time since bolometric maximum for our grid of SNe IIb/Ib/Ic models. The ratio at bolometric maximum has a mean of 1.41 and a standard deviation of σ =0.072. The shaded area corresponds to the mean ±σ.

Considering heating from radioactive decay and cooling through expansion and radiation, one can solve the internal energy equation out to late times to find

$$\int_{t_0}^{t} dt' t' E(t') = \int_{t_0}^{t} dt' t' L_{\rm dec}(t') - \int_{t_0}^{t} dt' t' L_{\rm bol}(t') \,, \qquad (1)$$

where $E(t')$ is the total radiation energy trapped within the ejecta at t' and $L_{\rm dec}$ is the total decay power (Katz et al. use instead the total decay energy deposited within the ejecta, but this quantity is not known directly). At late times, as the ejecta becomes optically thin, there is essentially no stored radiation energy so we neglect the associated term $tE(t)$. When evaluating this ratio for the CMFGEN simulation, we use t_0 = 3 d to skip the first few steps of the time sequences. In that case, we include the term $E(t_0)$, which is of the order of $\lesssim 10^{48}$ erg at that time in our models.

In Dessart et al. (2015), we found that the ratio

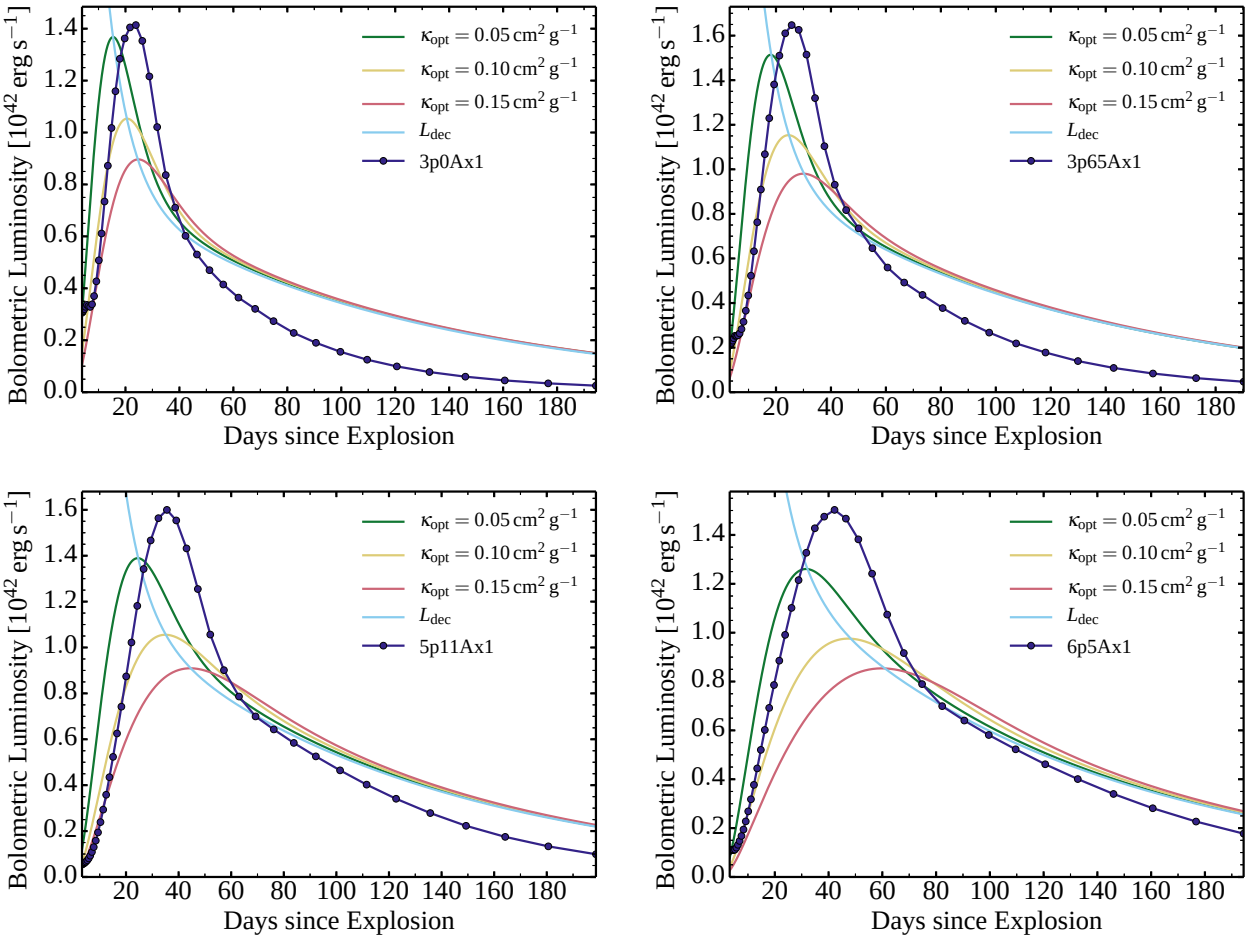

Figure 19. Comparison between the bolometric luminosity light curve for models 3p0Ax1, 3p65Ax1, 5p11Ax1, and 6p5Ax1, the total ^{56}Ni decay power, and the predictions of the Arnett model (Arnett 1982; Valenti et al. 2008) (we use the formulation of Valenti et al. 2008 but corrected for an error in the expression of $B(t)$ and s; see our Appendix D.) using three different values of $\kappa_{\rm opt}$ (to save space, we omit model 4p64Ax1). In each case, we use the ejecta kinetic energy, mass and ^{56}Ni mass of the CMFGEN model. The value $\kappa_{\rm opt} = 0.05\,{\rm cm^2\,g^{-1}}$ used by Drout et al. (2011) for their SNe Ibc study underestimates the rise time in all 5 cases, while the Arnett model overestimates the ^{56}Ni mass by up to a factor of two (Figure 18).

$\int_{t_0}^{t} dt' t' L_{\rm bol}(t')[\int_{t_0}^{t} dt' t' L_{\rm dec}(t') + t_0 E(t_0)]$ was within $\sim$1% of unity at 10-20 d after maximum for our three selected models. In these cases, γ-ray escape was negligible up to 10-20 d after maximum, and the convergence of the ratio to unity demonstrated instead the good energy conservation of the CMFGEN model.

Figure 17 shows this ratio for the full grid of models. As before, many models reach unity at 10-20 d after bolometric maximum. However, some do not, because γ-rays from radioactive decay start escaping the ejecta before it is optically-thin to optical photons. This is the case for lower mass ejecta and/or higher energy explosions. Stronger mixing also exacerbates the effect since it biases the ^{56}Ni distribution toward higher-velocity lower-density regions. The impact of γ-ray escape can be seen directly from the post-maximum decline rate (Figs. 2–3).

6.2 The Arnett model

A common expedient in the SN community is to apply the Arnett model (Arnett 1982), originally developed for SNe Ia, to all Type I SN light curves.

One feature of this model is the prediction that the bolometric luminosity at maximum is close to the instantaneous decay rate at that time. Hence, knowledge of the distance and reddening to a given SN Ia gives the ^{56}Ni mass needed to match the peak luminosity. For SNe Ia, detailed radiative-transfer calculations suggest that this relation is fairly accurate (see, e.g., Blondin et al. 2013), despite the various simplifications.

In Dessart et al. (2015), we found that the agreement is poorer when applied to SNe IIb/Ib/Ic. When the comparison is extended to our full grid of models, the disagreement is not reduced (Figure 18). Applying Arnett rule to our SN IIb/Ib/Ic models would lead to an overestimate of the ^{56}Ni mass by as much as 50%. In our simulations, $L_{\rm bol}/L_{\rm dec}$ has a mean of 1.41 and a standard deviation of 0.072. The offset found in Dessart et al. (2015) for a few models is therefore present in the larger set of models.

The adopted mixing plays a minor role (see Paper I, Section 6, where the influence of mixing is discussed for model 3p65A, 5p11A, and 6p5A, as well as Dessart et al. (2012) for an extended discussion of the impact of mixing in SNe Ibc light curves and spectra). In our models, enhanced mixing shortens the rise to bolometric maximum and enhances weakly the peak luminosity (all else being the same). For example, for model 3p65Ax1 (moderate mixing),

$L_{\rm bol}/L_{\rm dec}$ is 1.5. In model 3p65Ax2 (strong mixing), the bolometric maximum is a fraction of a percent higher but $L_{\rm bol}/L_{\rm dec}$ is only 1.42. The reduction in the offset between $L_{\rm bol}$ and $L_{\rm dec}$ is related to the shorter rise time of 1.5 d — the instantaneous decay power for the ^{56}Ni chain drops by 5% in 1.5 d at 20-25 d after explosion. As a reminder, in the absence of mixing, models also show a 40-50% offset between $L_{\rm bol}$ and $L_{\rm dec}$ at bolometric maximum (see Figure 13 of Dessart et al. 2011).

Let us now compare the CMFGEN bolometric light curve to the Arnett light-curve model (we use the formulation of Valenti et al. 2008, but we corrected the expressions of $B(t)$ and s; see our Appendix D.) This model has four unknowns: $M_{\rm e}$, $E_{\rm kin}$, M(^{56}Ni), and the mass-absorption coefficient for low-energy photons $\kappa_{\rm opt}$. We focus on the first part of the light curve, around maximum, and assume full γ-ray trapping. Using the values of $M_{\rm e}$, $E_{\rm kin}$, and $M(^{56}{\rm Ni})$ in a CMFGEN model, we can compare the Arnett model light curve to the CMFGEN result. The standard implementation of the Arnett model assumes a fixed opacity, while CMFGEN works from physical ejecta models and computes the opacity frequency-by-frequency and at all ejecta locations. This microphysics is treated entirely differently and there is no simple way to import the CMFGEN opacity into the Arnett model. So, we show the predictions of the Arnett model for three different values of $\kappa_{\rm opt}$.

Figure 19 shows that the central peak of the light curve from the Arnett model has the same qualitative shape but with an offset in all cases.[1] The maximum value is systematically under-estimated (see above). The post-breakout plateau is absent. The width of the light curve is better matched for models with a smaller $\kappa_{\rm opt}$, but the rise time to bolometric maximum is then underestimated. Larger values of $\kappa_{\rm opt}$ help resolving these deficiencies but the offset at bolometric maximum is increased. We can improve the match of the Arnett model to the bolometric light curve peak of model 3p65Ax1 computed by CMFGEN if we shift the Arnett light curve by 8 d and increase the ^{56}Ni mass by 10%. The time shift is needed to account for the post-breakout plateau predicted in our CMFGEN simulation and absent in the Arnett model. This manipulation is very artificial and this exercise merely illustrative.

If the SN light curve is entirely powered by ^{56}Ni power, then the Arnett model should give a good match to the energy criterion expressed in Katz et al. (2013). Figure 20 reproduces Figure 17 but for models 3p65Ax1 and 6p5Ax1 together with their Arnett model counterpart — we use the same $M_{\rm e}$, $E_{\rm kin}$, and M(^{56}Ni) as the CMFGEN model and cover three different values of $\kappa_{\rm opt}$. When the CMFGEN model reaches unity, the Arnett model is at $\sim$0.9, and even less for higher values of $\kappa_{\rm opt}$.

The Arnett model makes a number of simplifications. It assumes a progenitor star with a negligible radius. This is roughly equivalent to dropping the term $E(t_0)$ in the Katz ratio. In models 3p65Ax1 and 6p5Ax1, the total radiation energy stored within the ejecta at 3 d is 6–9$\times$ 10^{47} erg. In practice, neglecting that term changes the ratio at the 1% level, so this simplification is adequate. The Arnett model neglects ionization/excitation energy but this energy contribution is subdominant — it also affects the ratio at the 1% level. A feature of greater significance is the assumption of a fixed opacity. Figure 19 shows how sensitive the Arnett model light curve is to different values of this adopted opacity — this an inherent limitation of the Arnett model since the value to use is unknown.

[1] There is an obvious offset at late times because we assume full γ-ray trapping in the Arnett model but allow for γ-ray escape in the CMFGEN calculations

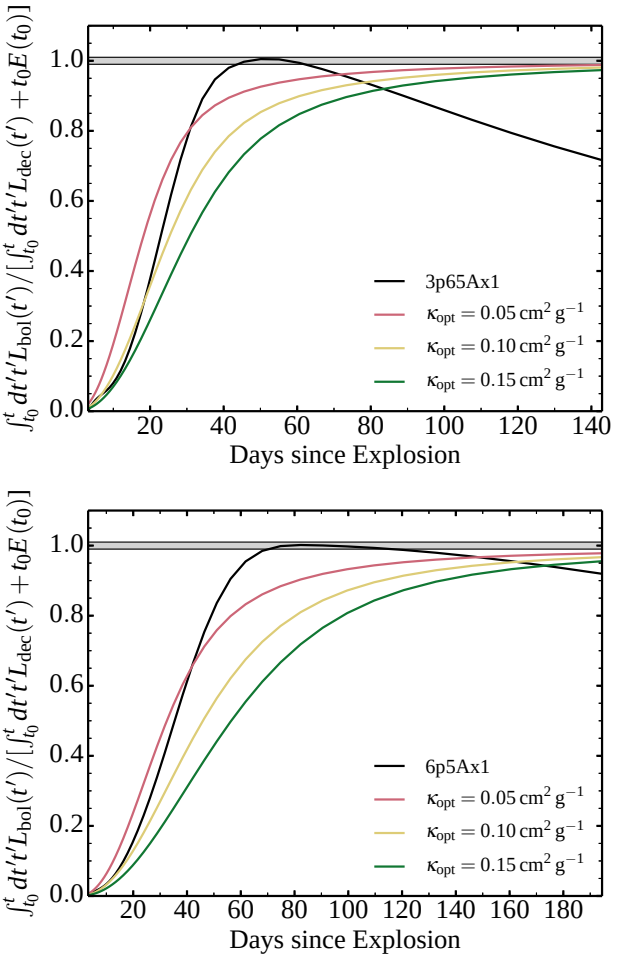

Figure 20. Illustration of the variation of the ratio $\int_{t_0}^{t} dt' t' L_{\rm bol}(t') / [\int_{t_0}^{t} dt' t' L_{\rm dec}(t') + t_0 E(t_0)]$ versus time since bolometric maximum (we use $t_0 \gtrsim 3$ d) for our models 3p65Ax1 and 6p5Ax1 together with the predictions from Arnett's model using three different values of $\kappa_{\rm opt}$ (for these curves, we use $t_0 = 0$ d). The ejecta kinetic energy, mass and ^{56}Ni mass are taken from the corresponding CMFGEN model. In the present implementation of the Arnett model we assume full γ-ray trapping so the curves rise to unity at late times. When unity is reached in the CMFGEN model, the Arnett model is at around 0.9 and the offset is larger for larger values of $\kappa_{\rm opt}$. One reason for the offset between the standard Arnett model predictions and the more detailed calculations with CMFGEN is the simplified treatment of the opacity.

Figure 21 shows the complicated behaviour of the opacity in our SN Ibc simulations. In reality, the opacity varies significantly both in space and time. Assuming a uniform and fixed opacity tends to underestimate the opacity in the inner ejecta and to overestimate it in the outer ejecta, which becomes essentially transparent very early on. This may be the main reason for the offset between the Arnett model light curve and the CMFGEN results.

7 CONCLUSIONS

This paper is a follow-up to Dessart et al. (2015), which focused on three models of type IIb, Ib, and Ic. Here, we extend our analysis to a large grid of models for SNe IIb/Ib/Ic that result from the terminal explosion of the mass donor in a close-binary system. All our re-

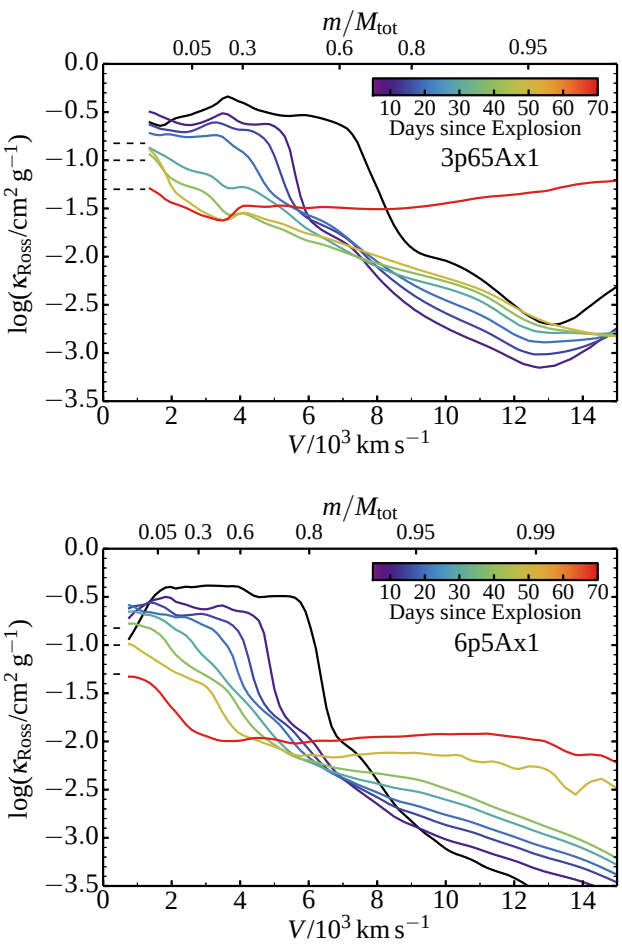

Figure 21. Evolution of the Rosseland-mean opacity versus velocity and time for model 3p65Ax1 and 6p5Ax1. The times shown are 5, 10, 15, 20, 30, 40, 50, and 70 d after explosion. For reference, we add marks on the left to locate $\kappa_{\rm Ross}$ values of 0.05, 0.10, and 0.15 cm^2 g^{-1} (to be compared to the values of $\kappa_{\rm opt}$ used in the Arnett model).

sults are based on 1-D non-LTE time-dependent radiative-transfer simulations with CMFGEN.

With this grid, we cover ejecta masses in the range 1.7–5.2 M$_\odot$, kinetic energies in the range 0.6–5.0$\times$10^{51} erg, and ^{56}Ni masses in the range 0.05–0.30 M$_\odot$. Equipped with better physics (non-thermal processes, improved model atoms) compared to Dessart et al. (2011), this sample also covers a much bigger parameter space than the focused study of Dessart et al. (2012) on chemical mixing. The range of progenitor (mass, composition, radius) and explosion properties (energy, ^{56}Ni mass) is by definition limited but hopefully this range overlaps significantly with the SNe IIb/Ib/Ic in Nature. Nonetheless, our approach allows a direct confrontation of observables (e.g., bolometric luminosity) to initial progenitor/ejecta properties (ejecta mass, ^{56}Ni mass). Even if limited, this controlled experiment yields interesting insights into the properties of SN IIb/Ib/Ic models, with, hopefully, relevance to SNe IIb/Ib/Ic in Nature.

A number of correlations emerge from this larger sample of models, which confirm some of the results presented in Dessart et al. (2015). As expected, we find a strong correlation between the ^{56}Ni mass and the maximum bolometric luminosity and peak brightness. We provide fitted formulae over the ^{56}Ni mass range 0.05–0.30 M$_\odot$. Our predictions at large ^{56}Ni mass are influenced by the large ejecta masses of the corresponding models. Ejecta with a larger kinetic energy mimic the behaviour of ejecta with a lower mass, confirming the general degeneracy of light curve morphology for a given $E_{\rm kin}/M_{\rm e}$. When considering the entire model set, however, we obtain a significant scatter in correlations involving $E_{\rm kin}/M_{\rm e}$ (or $V_{\rm m}$). Varying $E_{\rm kin}$ ($M_{\rm e}$) influences the rise time to maximum, the light curve width, the early post-maximum decline, and the nebular decline rate.

Across a wide range of $E_{\rm kin}$, $M_{\rm e}$, and $M(^{56}{\rm Ni})$, we find that the rise time to maximum strongly correlates with the post-maximum decline. We provide a correlation for the R band. This property can help estimate the explosion time when early time observations are lacking. It also alleviates the difficulty of securing such observations because SNe IIb/Ib/Ic are often very faint one day after explosion and until ^{56}Ni heating manifests itself.

A notorious problem for all type I SNe is the determination of the reddening. Indeed, unlike SNe II-Plateau, continuum windows free of lines are lacking and the effects of line blanketing are much stronger at all times, so a direct constraint on reddening is non trivial in type I SNe. However, the properties (composition, ionisation, temperature) of the spectrum formation region are quite similar in our models after maximum, which conspires to produce roughly the same intrinsic colour. In our set, the distribution of the $(V-R)$ colour at 10 d after R-band maximum has a mean of 0.33 mag, with a standard deviation of 0.035 mag. Observationally, a comparable estimate was made by Drout et al. (2011).

Spectral line morphology evolves with time as the spectrum formation region recedes in mass space, and therefore in velocity space. This is generally true for intermediate mass elements (C, O, Ca) but there are notable exceptions. In SNe IIb, the Doppler velocity at maximum absorption in Hα converges around maximum light to a value that corresponds to the velocity at the base of the H-rich shell in the outer ejecta (the line absorption appears as a stationary dip blue-ward of the rest wavelength). In our models, this velocity is always very large (in the range 8000–15000 km s^{-1}) because at most 0.01 M$_\odot$ of H remains in the progenitor star at the time of explosion.

In most models we identify a reversal in the trajectory followed by the maximum absorption in the He I 10830 Å line around the time of maximum brightness. This feature is unique to helium because He I is very sensitive to non-thermal excitation, which is intimately tied to the influence of γ-rays. In the outer ejecta where the ^{56}Ni mass fraction is small, this influence is weak early on, but strengthens around maximum as the γ-ray mean free path becomes comparable to the SN radius. The reversal affects the behaviour of the absorption seen around 10300 Å, and it is due to He I alone. Hence, this feature could serve as a test of the presence of helium in SNe Ic. This reversal is, however, weak or absent in strongly mixed models.

Determining the mean expansion rate of SN ejecta is a critical step in constructing a suitable model of the event. This is more meaningful than determining the photospheric velocity, which varies with time and depends on the selected line. In Dessart et al. (2015), we studied the evolution of the strongest optical and near-IR lines and confronted the value of the Doppler velocity at maximum absorption with the expansion rate $V_{\rm m}$ defined as $\sqrt{2E_{\rm kin}/M_{\rm e}}$. The complicated processes that influence SN IIb/Ib/Ic spectra do not allow a very accurate determination of $V_{\rm m}$. Nonetheless, we find that at light curve maximum, $V_{\rm m}$ is close to the measured value of the Doppler velocity at maximum absorption in He I 5875 Å in our SNe IIb/Ib models. For SNe Ic, one may use

O I 7772 Å, although the correspondence deteriorates with higher ejecta mass/energy.

Finally, we find that the Arnett model, originally designed for SNe Ia, is not very accurate when applied to SNe IIb/Ib/Ic. There may be a combination of factors. We suspect the main shortcoming is the assumption of a fixed opacity. The Arnett model light curve depends strongly on that adopted opacity, which is somewhat arbitrarily supplied by the user. There is in practice no good representative value, because the opacity varies with both ejecta location and age in SNe IIb/Ib/Ic. Assuming a fixed average opacity systematically overestimates the true opacity of the outer regions because these continuously recombine and turn transparent as they do so. The large helium mass fraction contributes to the low opacity of the outer ejecta. This transparent region grows in mass until the whole ejecta turns nebular. In the inner ejecta, the opacity varies with time too, as the ionisation changes and the sources of line blanketing evolve. This complicated time and spatial dependences of the opacity are ignored in the Arnett model and this simplification may compromise the rise time to maximum and the light curve width.

The next step with this work is to compare our models to observed SNe IIb, Ib, Ic.

ACKNOWLEDGMENTS

LD acknowledges financial support from the European Community through an International Re-integration Grant, under grant number PIRG04-GA-2008-239184, and from "Agence Nationale de la Recherche" grant ANR-2011-Blanc-SIMI-5-6-007-01. DJH acknowledges support from STScI theory grant HST-AR-12640.01, and NASA theory grant NNX14AB41G. SW was supported by NASA (NNX14AH34G) and the DOE High Energy Physics Program (DE-SC-00010676). SCY was supported by the Basic Science Research (2013R1A1A2061842) program through the National Research Foundation of Korea (NRF). This work was granted access to the HPC resources of CINES under the allocations c2013046608 and c2014046608 made by GENCI (Grand Equipement National de Calcul Intensif). This work also utilised computing resources of the Mésocentre SIGAMM, hosted by the Observatoire de la Côte d'Azur, Nice, France.

REFERENCES

Anderson, J. P., Covarrubias, R. A., James, P. A., Hamuy, M., & Habergham, S. M. 2010, MNRAS, 407, 2660
Anderson, J. P., Habergham, S. M., James, P. A., & Hamuy, M. 2012, MNRAS, 424, 1372
Anderson, J. P. & James, P. A. 2008, MNRAS, 390, 1527
—. 2009, MNRAS, 399, 559
Arcavi, I., Gal-Yam, A., Kasliwal, M. M., Quimby, R. M., Ofek, E. O., Kulkarni, S. R., Nugent, P. E., Cenko, S. B., Bloom, J. S., Sullivan, M., Howell, D. A., Poznanski, D., Filippenko, A. V., Law, N., Hook, I., Jönsson, J., Blake, S., Cooke, J., Dekany, R., Rahmer, G., Hale, D., Smith, R., Zolkower, J., Velur, V., Walters, R., Henning, J., Bui, K., McKenna, D., & Jacobsen, J. 2010, ApJ, 721, 777
Arnett, W. D. 1982, ApJ, 253, 785
Bautista, M. A. 2004, A&A, 420, 763
Bersten, M. C., Benvenuto, O. G., Nomoto, K., Ergon, M., Folatelli, G., Sollerman, J., Benetti, S., Botticella, M. T., Fraser, M., Kotak, R., Maeda, K., Ochner, P., & Tomasella, L. 2012, ApJ, 757, 31
Bianco, F. B., Modjaz, M., Hicken, M., Friedman, A., Kirshner, R. P., Bloom, J. S., Challis, P., Marion, G. H., Wood-Vasey, W. M., & Rest, A. 2014, ApJS, 213, 19
Blinnikov, S. I., Eastman, R., Bartunov, O. S., Popolitov, V. A., & Woosley, S. E. 1998, ApJ, 496, 454
Blondin, S., Dessart, L., Hillier, D. J., & Khokhlov, A. M. 2013, MNRAS, 429, 2127
Busche, J. R. & Hillier, D. J. 2005, AJ, 129, 454
Butler, K., Mendoza, C., & Zeippen, C. J. 1993, Journal of Physics B Atomic Molecular Physics, 26, 4409
Claeys, J. S. W., de Mink, S. E., Pols, O. R., Eldridge, J. J., & Baes, M. 2011, A&A, 528, A131
Crowther, P. A. 2013, MNRAS, 428, 1927
Cunto, W., Mendoza, C., Ochsenbein, F., & Zeippen, C. J. 1993, A&A, 275, L5
Dessart, L. & Hillier, D. J. 2010, MNRAS, 405, 2141
Dessart, L., Hillier, D. J., Blondin, S., & Khokhlov, A. 2014, MNRAS, 441, 3249
Dessart, L., Hillier, D. J., Li, C., & Woosley, S. 2012, MNRAS, 424, 2139
Dessart, L., Hillier, D. J., Livne, E., Yoon, S.-C., Woosley, S., Waldman, R., & Langer, N. 2011, MNRAS, 414, 2985
Dessart, L., Hillier, D. J., Woosley, S., Livne, E., Waldman, R., Yoon, S.-C., & Langer, N. 2015, MNRAS, 453, 2189
Drout, M. R., Soderberg, A. M., Gal-Yam, A., Cenko, S. B., Fox, D. B., Leonard, D. C., Sand, D. J., Moon, D.-S., Arcavi, I., & Green, Y. 2011, ApJ, 741, 97
Eldridge, J. J., Fraser, M., Smartt, S. J., Maund, J. R., & Crockett, R. M. 2013, MNRAS, 436, 774
Eldridge, J. J., Izzard, R. G., & Tout, C. A. 2008, MNRAS, 384, 1109
Ensman, L. M. & Woosley, S. E. 1988, ApJ, 333, 754
Ergon, M., Sollerman, J., Fraser, M., Pastorello, A., Taubenberger, S., Elias-Rosa, N., Bersten, M., Jerkstrand, A., Benetti, S., Botticella, M. T., Fransson, C., Harutyunyan, A., Kotak, R., Smartt, S., Valenti, S., Bufano, F., Cappellaro, E., Fiaschi, M., Howell, A., Kankare, E., Magill, L., Mattila, S., Maund, J., Naves, R., Ochner, P., Ruiz, J., Smith, K., Tomasella, L., & Turatto, M. 2014, A&A, 562, A17
Fernley, J. A., Hibbert, A., Kingston, A. E., & Seaton, M. J. 1999, Journal of Physics B Atomic Molecular Physics, 32, 5507
Filippenko, A. V., Porter, A. C., & Sargent, W. L. W. 1990, AJ, 100, 1575
Fryxell, B., Arnett, D., & Mueller, E. 1991a, ApJ, 367, 619
Fryxell, B., Arnett, D., & Müller, E. 1991b, ApJ, 367, 619
Groh, J. H., Meynet, G., Georgy, C., & Ekström, S. 2013, A&A, 558, A131
Harkness, R. P., Wheeler, J. C., Margon, B., Downes, R. A., Kirshner, R. P., Uomoto, A., Barker, E. S., Cochran, A. L., Dinerstein, H. L., Garnett, D. R., & Levreault, R. M. 1987, ApJ, 317, 355
Hillier, D. J. & Dessart, L. 2012, MNRAS, 424, 252
Hillier, D. J. & Miller, D. L. 1998, ApJ, 496, 407
Hummer, D. G., Berrington, K. A., Eissner, W., Pradhan, A. K., Saraph, H. E., & Tully, J. A. 1993, A&A, 279, 298
Janka, H.-T., Hanke, F., Hüdepohl, L., Marek, A., Müller, B., & Obergaulinger, M. 2012, Progress of Theoretical and Experimental Physics, 2012, 010000
Katz, B., Kushnir, D., & Dong, S. 2013, arXiv:1301.6766
Kelly, P. L. & Kirshner, R. P. 2012, ApJ, 759, 107
Kim, H.-J., Yoon, S.-C., & Koo, B.-C. 2015, ApJ, 809, 131

Kramida, A. E., Ralchenko, Y., Reader, J., & NIST ASD Team. 2012, NIST Atomic Spectra Database (version 5.0)
Kurucz, R. L. 2009, in American Institute of Physics Conference Series, Vol. 1171, American Institute of Physics Conference Series, ed. I. Hubeny, J. M. Stone, K. MacGregor, & K. Werner, 43–51
Kurucz, R. L. 2010
Liu, Y.-Q., Modjaz, M., Bianco, F. B., & Graur, O. 2015, arXiv:1510.08049
Lucy, L. B. 1991, ApJ, 383, 308
Luo, D. & Pradhan, A. K. 1989, Journal of Physics B Atomic Molecular Physics, 22, 3377
Mendoza, C. 1983, in IAU Symposium, Vol. 103, Planetary Nebulae, ed. D. R. Flower, 143–172
Mendoza, C., Eissner, W., LeDourneuf, M., & Zeippen, C. J. 1995, Journal of Physics B Atomic Molecular Physics, 28, 3485
Modjaz, M., Kewley, L., Bloom, J. S., Filippenko, A. V., Perley, D., & Silverman, J. M. 2011, ApJL, 731, L4
Nadyozhin, D. K. 1994, ApJS, 92, 527
Nahar, S. N. & Pradhan, A. K. 1993, Journal of Physics B Atomic Molecular Physics, 26, 1109
—. 1994, Journal of Physics B Atomic Molecular Physics, 27, 429
Nussbaumer, H. & Storey, P. J. 1983, A&A, 126, 75
—. 1984, A&AS, 56, 293
Podsiadlowski, P., Joss, P. C., & Hsu, J. J. L. 1992, ApJ, 391, 246
Ralchenko, Y., Kramida, A. E., Reader, I., & NIST ASD Team. 2010, NIST Atomic Spectra Database (version 3.1.5)
Sanders, N. E., Soderberg, A. M., Levesque, E. M., Foley, R. J., Chornock, R., Milisavljevic, D., Margutti, R., Berger, E., Drout, M. R., Czekala, I., & Dittmann, J. A. 2012, ApJ, 758, 132
Sauer, D. N., Mazzali, P. A., Deng, J., Valenti, S., Nomoto, K., & Filippenko, A. V. 2006, MNRAS, 369, 1939
Seaton, M. J. 1987, Journal of Physics B Atomic Molecular Physics, 20, 6363
Shine, R. A. & Linsky, J. L. 1974, Solar Physics, 39, 49
Smith, N., Li, W., Filippenko, A. V., & Chornock, R. 2011, MNRAS, 412, 1522
Sukhbold, T., Ertl, T., Woosley, S. E., Brown, J. M., & Janka, H.-T. 2015, arXiv:1510.04643
Sunderland, A. G., Noble, C. J., Burke, V. M., & Burke, P. G. 2002, Computer Physics Communications, 145, 311
Tachiev, G. I. & Froese Fischer, C. 2002, A&A, 385, 716
Ugliano, M., Janka, H.-T., Marek, A., & Arcones, A. 2012, ApJ, 757, 69
Valenti, S., Benetti, S., Cappellaro, E., Patat, F., Mazzali, P., Turatto, M., Hurley, K., Maeda, K., Gal-Yam, A., Foley, R. J., Filippenko, A. V., Pastorello, A., Challis, P., Frontera, F., Harutyunyan, A., Iye, M., Kawabata, K., Kirshner, R. P., Li, W., Lipkin, Y. M., Matheson, T., Nomoto, K., Ofek, E. O., Ohyama, Y., Pian, E., Poznanski, D., Salvo, M., Sauer, D. N., Schmidt, B. P., Soderberg, A., & Zampieri, L. 2008, MNRAS, 383, 1485
van Regemorter, H. 1962, ApJ, 136, 906
Wheeler, J. C., Harkness, R. P., Barker, E. S., Cochran, A. L., & Wills, D. 1987, ApJL, 313, L69
Wheeler, J. C. & Levreault, R. 1985, ApJL, 294, L17
Wongwathanarat, A., Mueller, E., & Janka, H.-T. 2015, A&A, 577, A48
Woosley, S. E., Langer, N., & Weaver, T. A. 1995, ApJ, 448, 315
Yoon, S., Woosley, S. E., & Langer, N. 2010, ApJ, 725, 940
Yoon, S.-C., Gräfener, G., Vink, J. S., Kozyreva, A., & Izzard, R. G. 2012, A&A, 544, L11
Zhang, H. 1996, A&AS, 119, 523
Zhang, H. L. & Pradhan, A. K. 1994, VizieR Online Data Catalog, 329, 30953
—. 1995a, A&A, 293
—. 1995b, Journal of Physics B Atomic Molecular Physics, 28, 3403

APPENDIX A: DETAILS ON THE RADIATIVE TRANSFER CALCULATIONS AND THE ATOMIC DATA

The radiation code CMFGEN (Hillier & Miller 1998), is used to determine the atomic level populations. In these calculations we assume a 1-D homologous expansion, although we have routines available that relax this assumption. We solve the transfer equation in the comoving-frame as discussed by Hillier & Dessart (2012), and we explicitly allow for the time dependence of the radiation field. To obtain the Eddington factors, we perform a formal solution in which time dependence is neglected. As we explicitly treat the time dependence with the moment equations, and since the Eddington factors are ratios of moments, this approximation has only a minor influence on the calculations. The assumption of 1D is an approximation and there is ample observational and theoretical evidence, especially for core collapse SNe, that multi-dimensional effects are important (see review by Janka et al. 2012). A related effect, that can influence the results, is mixing. As the mixing is likely macroscopic, and not microscopic (Fryxell et al. 1991a), it cannot be easily treated in 1-D calculations. Given the huge computational costs associated with full 3-D non-LTE time-dependent calculations, and our still limited understanding of SN ejecta, 1-D calculations are an essential analysis tool.

We compute the observer's spectrum in two ways. First, we compute the spectrum with the CMFGEN calculation. To do this we perform a Lorentz transformation of the outer boundary comoving-frame intensities, and then integrate them in the usual way to obtain the observed flux. In the second method we use a separate code, CMF_FLUX (Busche & Hillier 2005). In this code we first solve for the radiation field, similar to the CMFGEN calculation. However we include all bound-bound transitions in our model atoms, and typically use finer frequency and spatial grids. The CMF calculation provides the mean intensity J which is used to compute the electron scattering emissivity. We then perform a formal solution in the Observer's frame utilising Lorentz transforms of the comoving emissivities and opacities. In general spectra computed by the two methods are in excellent agreement.

An explicit assumption of our approach is that the light-travel time effects are small. We cannot accurately model SN when rapid changes are occurring, such as at shock breakout. That is, we can not accurately model the spectrum for events changing faster than a timescale of $R_{\rm phot}/c$.

An essential requirement of the calculations is accurate atomic data, and since we are performing non-LTE calculations we require gf values, energy levels, accurate wavelengths, collisional data, photo-ionisation cross-sections, auto-ionising data, and charge exchange cross-sections. The quality of the available data varies considerably with the atomic species, and the complexity of the electronic configuration. When available, we use accurate energy levels, as obtained from the NIST website (Kramida et al. 2012; Ralchenko et al. 2010) (sometimes indirectly from NIST as Robert Kurucz uses accurate energies in his calculations when they are available). For Fe group elements not all levels are known (particularly for highly excited levels, and for elements other than Fe), and in that case we use energy levels calculated by Kurucz (Kurucz

2009, 2010). These energy levels lead to inaccurate wavelengths although in our SNe calculations our results do not reveal a major problem when using inaccurate wavelengths. In the CMF_FLUX calculations we have the ability to omit transitions with unknown wavelengths.

For H and He the atomic data is excellent. For CNO the data is also of high quality, and the data for elements with atomic number up to $Z = 20$ is also reasonable. In general reasonable atomic data is available for Fe, but for the other Fe group elements much less data is available. Due to the complexity of their electronic configuration, the data quality for Fe (and other Fe group elements when available) is generally of lower quality than that of CNO.

Oscillator strengths are available from a wide a variety of sources such as the Opacity Project (Seaton 1987) and the Fe project (Hummer et al. 1993), and most are theoretical. Because of their completeness, extensive use is made of the calculations by Kurucz (Kurucz 2009, 2010). For some species oscillator strengths have been updated with values from NIST (Kramida et al. 2012; Ralchenko et al. 2010). When available, we use theoretical collisional data from the literature. For many species such data is unavailable, and we use the approximate values obtained from the expression of van Regemorter (van Regemorter 1962). Photoionisation cross section of elements with $Z \leqslant 26$ (and Z even) are available through the Opacity Project (Seaton 1987), the Fe project (Hummer et al. 1993) and through many other calculations.[2] A potential drawback of these calculations is that the resonances are not at the correct wavelengths, and are treated in LS coupling. This can affect spectral comparisons, and potentially could influence non-LTE calculations through the incorrect treatment of overlapping spectral features. For many species, such as Co, accurate photoionisation data is unavailable. In such cases we use approximations.

In addition to the primary sources listed above, the atomic data for the present calculations were taken from Shine & Linsky (1974), Mendoza (1983), Nussbaumer & Storey (1983), Nussbaumer & Storey (1984), Luo & Pradhan (1989), Cunto et al. (1993), Nahar & Pradhan (1993), Butler et al. (1993), Zhang & Pradhan (1994), Nahar & Pradhan (1994), Mendoza et al. (1995), Zhang & Pradhan (1995a), Zhang & Pradhan (1995b), Zhang (1996), Fernley et al. (1999), Sunderland et al. (2002), Tachiev & Froese Fischer (2002), and Bautista (2004).

Due to the complexity of non-LTE calculations it is difficult to gauge the influence of poor atomic data on the calculations. We do run sensitivity tests to the size of the atomic models, and in some cases to the atomic data (for those cases where we have multiple data sets). For many SN models we get consistent fits across many epochs, and since the sensitivities to the atomic data are changing with the SN epoch (since the physical conditions are changing), this suggests that uncertainties in the atomic data are not having a major influence (at least qualitatively). However we have had occurrences where the neglect of certain atomic data has had a major influence on the calculations (Dessart et al. 2014).

APPENDIX B: MODEL PROPERTIES FOR THE FULL SAMPLE

In this section, we present a summary of the model properties. Table B1 gives some progenitor and ejecta masses for the full grid of 27 models. Table B2 provides the ejecta yields for the dominant species. Table B3 gives the composition of some important species in the outermost ejecta layers (i.e., at the progenitor surface).

APPENDIX C: PHOTOMETRIC CHARACTERISTICS

Tables C1–C2–C3 give a summary of the photometric properties of our grid of models, including the rise time, value at maximum brightness, and post-maximum decline for the bolometric luminosity, the luminosity falling between 1000 Å and 2.5 μm ($L_{\rm UVOIR}$, and the photometric bands U, B, V, R, I, J, H, and $K_{\rm s}$.

APPENDIX D: EXPRESSION OF THE BOLOMETRIC LUMINOSITY

In Section 6.2, we plot the bolometric luminosity from the Arnett model and compare it to the CMFGEN results. Arnett (1982) provides an expression for the bolometric luminosity that includes the contribution from ^{56}Ni alone. Valenti et al. (2008) extend this expression to also treat ^{56}Co decay, but we find two errors in their expressions. Below, we provide the various terms entering the expression that we use for the bolometric luminosity in the Arnett model.

For the mean lifetimes and decay energies of ^{56}Ni and ^{56}Co, we use (Nadyozhin 1994; Valenti et al. 2008):

$$\tau_{\rm Ni} = 6.0749/\log 2 \ \ {\rm d}\,, \tag{D1}$$

$$\tau_{\rm Co} = 77.233/\log 2 \ \ {\rm d}\,, \tag{D2}$$

$$\epsilon_{\rm Ni} = 3.9 \times \ 10^{10}\,{\rm erg\,g^{-1}\,s^{-1}}\,, \tag{D3}$$

$$\epsilon_{\rm Co} = 6.78 \times 10^{9}\,{\rm erg\,g^{-1}\,s^{-1}}\,, \tag{D4}$$

Arnett (1982) defines the time scale $\tau_{\rm m}$ as

$$\tau_{\rm m} = \left(\frac{\kappa_{\rm opt}}{\beta c}\sqrt{\frac{10M_{\rm e}^3}{3E_{\rm kin}}}\right)^{1/2} \tag{D5}$$

and from Valenti et al. (2008) we use:

$$\beta = 13.8. \tag{D6}$$

Using Equation 31 of Arnett (1982):

$$\Lambda(x,y) = \exp(-x^2)\int_0^x 2z\exp(-2zy+z^2)dz\ , \tag{D7}$$

and the following definitions for x, y, s, and w,

$$x = t/\tau_{\rm m}\ , \tag{D8}$$

$$y = 0.5\tau_{\rm m}/\tau_{\rm Ni}\ , \tag{D9}$$

$$s = 0.5\tau_{\rm m}/\tau_{\rm Co}\ , \tag{D10}$$

$$w = \tau_{\rm Co}/(\tau_{\rm Co}-\tau_{\rm Ni})\ , \tag{D11}$$

we find that the bolometric luminosity in the Arnett model is:

$$L_{\rm bol}(t) = M_{\rm Ni}\left(\left[\epsilon_{\rm Ni}-\omega\epsilon_{\rm Co}\right]\Lambda(x,y)+\omega\epsilon_{\rm Co}\Lambda(x,s)\right)\ , \tag{D12}$$

where $M_{\rm Ni}$ is the initial ^{56}Ni mass. This expression assumes full γ-ray trapping.

[2] For example, by the atomic data group at Ohio State University. The data from S. N. Nahar is available online at http://www.astronomy.ohiostate.edu/∼nahar/.

Table B1. Progenitor and ejecta properties. The last three columns give the ejecta velocity that bounds 99% of the corresponding species total mass. The integration is done inwards in velocity space for H and He, and outwards for ^{56}Ni.

Model	$M_{\rm i}$ [M$_\odot$]	$M_{\rm f}$ [M$_\odot$]	$R_\star$ [cm]	$M_{\rm r}$ [M$_\odot$]	$M_{\rm e}$ [M$_\odot$]	Z	$E_{\rm kin}$ [B]	$V_{99,\rm H}$ [km s^{-1}]	$V_{99,\rm He}$ [km s^{-1}]	$V_{99,\rm Ni}$ [km s^{-1}]
3p0Cx1	18.0	3.00	1.10(12)	1.29	1.71	0.02	0.62	1.19(4)	1.83(3)	6.07(3)
3p0Cx2	18.0	3.00	1.10(12)	1.29	1.71	0.02	0.62	1.10(4)	1.64(3)	9.06(3)
3p0Ax1	18.0	3.00	1.10(12)	1.27	1.73	0.02	1.25	1.68(4)	2.84(3)	6.91(3)
3p0Ax2	18.0	3.00	1.10(12)	1.28	1.72	0.02	1.24	1.58(4)	2.47(3)	1.06(4)
3p0Bx2	18.0	3.00	1.10(12)	1.27	1.73	0.02	2.50	2.30(4)	3.73(3)	1.21(4)
3p65Cx1	16.0	3.65	1.17(12)	1.46	2.19	0.02	0.61	9.11(3)	1.91(3)	6.01(3)
3p65Cx2	16.0	3.65	1.17(12)	1.47	2.18	0.02	0.61	8.43(3)	1.63(3)	8.61(3)
3p65Ax1	16.0	3.65	1.17(12)	1.42	2.23	0.02	1.24	1.32(4)	3.03(3)	6.85(3)
3p65Ax2	16.0	3.65	1.17(12)	1.43	2.22	0.02	1.22	1.24(4)	2.62(3)	1.01(4)
3p65Bx2	16.0	3.65	1.17(12)	1.42	2.23	0.02	2.47	1.83(4)	4.00(3)	1.19(4)
3p65Dx2	16.0	3.65	1.17(12)	1.42	2.23	0.02	5.08	2.68(4)	4.40(3)	1.38(4)
4p64Cx1	18.0	4.64	1.10(12)	1.49	3.15	0.004	0.62	7.41(3)	2.03(3)	5.44(3)
4p64Ax1	18.0	4.64	1.10(12)	1.53	3.11	0.004	1.22	1.03(4)	3.46(3)	6.66(3)
4p64Ax2	18.0	4.64	1.10(12)	1.52	3.12	0.004	1.22	9.40(3)	2.79(3)	9.69(3)
4p64Bx1	18.0	4.64	1.10(12)	1.46	3.18	0.004	2.45	1.45(4)	3.71(3)	7.78(3)
4p64Bx2	18.0	4.64	1.10(12)	1.47	3.17	0.004	2.46	1.39(4)	4.48(3)	1.17(4)
4p64Dx2	18.0	4.64	1.10(12)	1.43	3.21	0.004	5.13	2.08(4)	4.67(3)	1.38(4)
5p11Ax1	60.0	5.11	5.19(10)	1.57	3.54	0.02	1.25	...	1.69(3)	6.00(3)
5p11Ax2	60.0	5.11	5.19(10)	1.49	3.62	0.02	1.29	...	2.71(3)	9.18(3)
5p11Bx1	60.0	5.11	5.19(10)	1.49	3.62	0.02	2.49	...	1.59(3)	7.08(3)
5p11Bx2	60.0	5.11	5.19(10)	1.48	3.63	0.02	2.49	...	1.74(3)	1.10(4)
6p5Ax1	25.0	6.50	2.01(11)	1.53	4.97	0.02	1.26	...	3.26(3)	5.94(3)
6p5Ax2	25.0	6.50	2.01(11)	1.55	4.95	0.02	1.25	...	2.55(3)	8.60(3)
6p5Bx1	25.0	6.50	2.01(11)	1.55	4.95	0.02	2.42	...	1.96(3)	6.57(3)
6p5Bx2	25.0	6.50	2.01(11)	1.52	4.98	0.02	2.43	...	3.38(3)	1.02(4)
6p5Gx1	25.0	6.50	2.01(11)	1.36	5.14	0.02	5.28	...	2.89(3)	8.91(3)
6p5Gx2	25.0	6.50	2.01(11)	1.32	5.18	0.02	5.30	...	3.09(3)	1.22(4)

Table B2. Cumulative yields for our grid of models at ~ 2 d after explosion. For ^{56}Ni, we give the original mass, i.e., prior to decay.

Model	H [$M_\odot$]	He [$M_\odot$]	C [$M_\odot$]	N [$M_\odot$]	O [$M_\odot$]	Si [$M_\odot$]	S [$M_\odot$]	Ca [$M_\odot$]	Fe [$M_\odot$]	^{56}Ni [$M_\odot$]
3p0Cx1	7.81(-4)	1.30(0)	5.48(-2)	1.15(-2)	1.18(-1)	6.21(-2)	2.48(-2)	2.36(-3)	2.05(-3)	3.87(-2)
3p0Cx2	7.81(-4)	1.30(0)	5.44(-2)	1.14(-2)	1.19(-1)	6.29(-2)	2.51(-2)	2.39(-3)	1.95(-3)	3.93(-2)
3p0Ax1	7.92(-4)	1.31(0)	5.48(-2)	1.15(-2)	1.24(-1)	5.63(-2)	2.12(-2)	2.60(-3)	2.54(-3)	5.78(-2)
3p0Ax2	7.73(-4)	1.31(0)	5.42(-2)	1.14(-2)	1.21(-1)	5.50(-2)	2.07(-2)	2.56(-3)	2.46(-3)	6.15(-2)
3p0Bx2	7.72(-4)	1.33(0)	5.39(-2)	1.15(-2)	1.19(-1)	4.93(-2)	2.00(-2)	3.32(-3)	2.78(-3)	7.02(-2)
3p65Cx1	4.74(-3)	1.47(0)	9.39(-2)	1.08(-2)	3.04(-1)	7.49(-2)	2.37(-2)	2.97(-3)	2.66(-3)	4.45(-2)
3p65Cx2	4.70(-3)	1.47(0)	9.31(-2)	1.08(-2)	3.04(-1)	7.57(-2)	2.39(-2)	3.00(-3)	2.64(-3)	4.50(-2)
3p65Ax1	4.99(-3)	1.49(0)	9.40(-2)	1.09(-2)	3.02(-1)	7.38(-2)	2.36(-2)	3.94(-3)	3.12(-3)	7.42(-2)
3p65Ax2	4.72(-3)	1.48(0)	9.37(-2)	1.08(-2)	3.01(-1)	7.30(-2)	2.33(-2)	3.91(-3)	3.13(-3)	7.66(-2)
3p65Bx2	4.95(-3)	1.51(0)	9.35(-2)	1.08(-2)	2.83(-1)	7.24(-2)	2.43(-2)	4.93(-3)	3.43(-3)	1.01(-1)
3p65Dx2	4.64(-3)	1.55(0)	9.33(-2)	1.07(-2)	2.51(-1)	7.64(-2)	2.86(-2)	5.48(-3)	3.60(-3)	1.05(-1)
4p64Cx1	1.66(-2)	1.72(0)	1.54(-1)	3.28(-3)	6.91(-1)	9.08(-2)	2.61(-2)	3.24(-3)	1.25(-3)	3.96(-2)
4p64Ax1	1.72(-2)	1.69(0)	1.48(-1)	3.23(-3)	6.85(-1)	9.35(-2)	2.65(-2)	3.58(-3)	1.42(-3)	6.20(-2)
4p64Ax2	1.70(-2)	1.69(0)	1.49(-1)	3.22(-3)	6.79(-1)	9.43(-2)	2.74(-2)	3.77(-3)	1.42(-3)	6.81(-2)
4p64Bx1	1.65(-2)	1.76(0)	1.52(-1)	3.26(-3)	6.75(-1)	1.01(-1)	2.66(-2)	4.90(-3)	2.44(-3)	8.76(-2)
4p64Bx2	1.67(-2)	1.75(0)	1.50(-1)	3.27(-3)	6.77(-1)	1.01(-1)	2.63(-2)	4.82(-3)	2.21(-3)	8.85(-2)
4p64Dx2	1.55(-2)	1.81(0)	1.50(-1)	3.28(-3)	6.44(-1)	1.18(-1)	3.42(-2)	6.15(-3)	2.29(-3)	1.09(-1)
5p11Ax1	0	3.15(-1)	8.92(-1)	0	1.42(0)	1.28(-1)	4.00(-2)	5.98(-3)	4.57(-3)	8.94(-2)
5p11Ax2	0	3.26(-1)	9.23(-1)	0	1.44(0)	1.28(-1)	4.04(-2)	6.13(-3)	4.69(-3)	9.46(-2)
5p11Bx1	0	3.37(-1)	8.86(-1)	0	1.40(0)	1.53(-1)	5.24(-2)	8.96(-3)	7.63(-3)	1.89(-1)
5p11Bx2	0	3.37(-1)	8.88(-1)	0	1.40(0)	1.53(-1)	5.21(-2)	8.88(-3)	7.83(-3)	1.88(-1)
6p5Ax1	0	1.67(0)	4.13(-1)	7.59(-3)	1.57(0)	2.12(-1)	9.31(-2)	9.30(-3)	6.19(-3)	9.90(-2)
6p5Ax2	0	1.66(0)	4.11(-1)	7.52(-3)	1.57(0)	2.14(-1)	9.40(-2)	9.51(-3)	6.31(-3)	1.02(-1)
6p5Bx1	0	1.61(0)	3.94(-1)	7.21(-3)	1.53(0)	2.09(-1)	8.99(-2)	1.12(-2)	1.10(-2)	2.44(-1)
6p5Bx2	0	1.62(0)	3.99(-1)	7.21(-3)	1.54(0)	2.08(-1)	8.97(-2)	1.12(-2)	1.08(-2)	2.42(-1)
6p5Gx1	0	1.79(0)	3.93(-1)	7.56(-3)	1.53(0)	2.16(-1)	8.36(-2)	1.33(-2)	1.34(-2)	2.89(-1)
6p5Gx2	0	1.78(0)	4.00(-1)	7.53(-3)	1.55(0)	2.17(-1)	8.38(-2)	1.34(-2)	1.31(-2)	2.88(-1)

Table B3. Mass fractions for some important species in the outermost mass shell for our grid of models. This shell corresponds to the progenitor surface.

Model	$X_{\rm H,s}$	$X_{\rm He,s}$	$X_{\rm C,s}$	$X_{\rm N,s}$	$X_{\rm O,s}$	$X_{\rm Si,s}$	$X_{\rm S,s}$	$X_{\rm Ca,s}$	$X_{\rm Fe,s}$
3p0Cx1	7.268(-2)	9.088(-1)	2.009(-4)	1.330(-2)	4.019(-4)	7.348(-4)	2.969(-4)	4.579(-5)	9.086(-4)
3p0Cx2	7.285(-2)	9.084(-1)	1.989(-4)	1.329(-2)	3.997(-4)	7.325(-4)	3.648(-4)	6.436(-5)	9.086(-4)
3p0Ax1	7.167(-2)	9.096(-1)	2.009(-4)	1.329(-2)	4.008(-4)	7.346(-4)	3.648(-4)	6.437(-5)	9.086(-4)
3p0Ax2	7.102(-2)	9.102(-1)	2.010(-4)	1.330(-2)	4.011(-4)	7.352(-4)	3.651(-4)	6.441(-5)	9.086(-4)
3p0Bx2	6.987(-2)	9.116(-1)	2.009(-4)	1.329(-2)	3.998(-4)	7.347(-4)	2.969(-4)	4.578(-5)	9.086(-4)
3p65Cx1	1.481(-1)	8.334(-1)	1.981(-4)	1.321(-2)	4.832(-4)	7.353(-4)	2.971(-4)	4.582(-5)	9.086(-4)
3p65Cx2	1.479(-1)	8.334(-1)	1.988(-4)	1.319(-2)	4.846(-4)	7.344(-4)	3.647(-4)	6.435(-5)	9.086(-4)
3p65Ax1	1.480(-1)	8.332(-1)	1.980(-4)	1.320(-2)	4.831(-4)	7.352(-4)	3.651(-4)	6.442(-5)	9.086(-4)
3p65Ax2	1.479(-1)	8.334(-1)	1.978(-4)	1.319(-2)	4.826(-4)	7.344(-4)	3.647(-4)	6.435(-5)	9.086(-4)
3p65Bx2	1.471(-1)	8.344(-1)	1.981(-4)	1.321(-2)	4.832(-4)	7.353(-4)	2.971(-4)	4.582(-5)	9.086(-4)
3p65Dx2	1.449(-1)	8.366(-1)	1.979(-4)	1.319(-2)	4.817(-4)	7.346(-4)	2.968(-4)	4.578(-5)	9.086(-4)
4p64Cx1	3.161(-1)	6.802(-1)	4.041(-5)	2.581(-3)	1.760(-4)	1.470(-4)	7.302(-5)	1.288(-5)	1.815(-4)
4p64Ax1	3.161(-1)	6.802(-1)	4.051(-5)	2.581(-3)	1.760(-4)	1.470(-4)	7.302(-5)	1.288(-5)	1.815(-4)
4p64Ax2	3.158(-1)	6.805(-1)	4.047(-5)	2.578(-3)	1.759(-4)	1.469(-4)	7.294(-5)	1.287(-5)	1.815(-4)
4p64Bx1	3.151(-1)	6.812(-1)	4.051(-5)	2.581(-3)	1.750(-4)	1.470(-4)	7.302(-5)	1.288(-5)	1.815(-4)
4p64Bx2	3.151(-1)	6.812(-1)	4.051(-5)	2.581(-3)	1.750(-4)	1.470(-4)	7.302(-5)	1.288(-5)	1.815(-4)
4p64Dx2	3.091(-1)	6.872(-1)	4.081(-5)	2.581(-3)	1.680(-4)	1.470(-4)	7.302(-5)	1.288(-5)	1.815(-4)
5p11Ax1	0	3.611(-1)	5.051(-1)	0	1.100(-1)	7.362(-4)	3.651(-4)	6.442(-5)	9.097(-4)
5p11Ax2	0	3.611(-1)	5.051(-1)	0	1.100(-1)	7.362(-4)	3.651(-4)	6.442(-5)	9.097(-4)
5p11Bx1	0	3.611(-1)	5.051(-1)	0	1.100(-1)	7.362(-4)	3.651(-4)	6.442(-5)	9.097(-4)
5p11Bx2	0	3.611(-1)	5.051(-1)	0	1.100(-1)	7.362(-4)	3.651(-4)	6.442(-5)	9.097(-4)
6p5Ax1	0	9.813(-1)	4.147(-4)	1.309(-2)	3.098(-4)	7.345(-4)	3.647(-4)	6.435(-5)	9.086(-4)
6p5Ax2	0	9.813(-1)	4.147(-4)	1.309(-2)	3.098(-4)	7.345(-4)	3.647(-4)	6.435(-5)	9.086(-4)
6p5Bx1	0	9.813(-1)	4.147(-4)	1.309(-2)	3.098(-4)	7.345(-4)	3.647(-4)	6.435(-5)	9.086(-4)
6p5Bx2	0	9.813(-1)	4.147(-4)	1.309(-2)	3.098(-4)	7.345(-4)	3.647(-4)	6.435(-5)	9.086(-4)
6p5Gx1	0	9.813(-1)	4.147(-4)	1.309(-2)	3.098(-4)	7.345(-4)	3.647(-4)	6.435(-5)	9.086(-4)
6p5Gx2	0	9.813(-1)	4.147(-4)	1.309(-2)	3.098(-4)	7.345(-4)	3.647(-4)	6.435(-5)	9.086(-4)

Table C1. Some light curves properties of our models. For each entry, we give the rise to maximum, the value at peak, and the magnitude change between peak and 15 d later.

Model	$L_{\rm bol}$			$L_{\rm UVOIR}$			U			B		
	$t_{\rm rise}$ [d]	Max. [erg s^{-1}]	ΔM_{15} [mag]	$t_{\rm rise}$ [d]	Max. [erg s^{-1}]	ΔM_{15} [mag]	$t_{\rm rise}$ [d]	Max. [mag]	ΔM_{15} [mag]	$t_{\rm rise}$ [d]	Max. [mag]	ΔM_{15} [mag]
3p0Cx1	2.530(1)	9.147(41)	6.837(-1)	2.499(1)	7.047(41)	7.784(-1)	2.366(1)	-1.494(1)	1.130(0)	2.378(1)	-1.587(1)	1.073(0)
3p0Cx2	2.375(1)	9.060(41)	7.124(-1)	2.359(1)	6.621(41)	7.309(-1)	2.221(1)	-1.449(1)	4.694(-1)	2.178(1)	-1.551(1)	6.891(-1)
3p0Ax1	2.296(1)	1.414(42)	7.221(-1)	2.263(1)	1.135(42)	8.486(-1)	2.092(1)	-1.577(1)	1.418(0)	2.141(1)	-1.655(1)	1.294(0)
3p0Ax2	2.228(1)	1.480(42)	7.401(-1)	2.214(1)	1.129(42)	7.936(-1)	2.178(1)	-1.535(1)	8.424(-1)	2.136(1)	-1.634(1)	1.009(0)
3p0Bx2	1.934(1)	1.818(42)	8.832(-1)	1.921(1)	1.417(42)	9.780(-1)	1.814(1)	-1.575(1)	8.646(-1)	1.829(1)	-1.674(1)	1.376(0)
3p65Cx1	2.826(1)	9.412(41)	5.636(-1)	2.770(1)	7.093(41)	6.352(-1)	2.437(1)	-1.484(1)	8.302(-1)	2.482(1)	-1.581(1)	8.027(-1)
3p65Cx2	2.665(1)	9.386(41)	5.389(-1)	2.630(1)	6.787(41)	5.361(-1)	2.559(1)	-1.449(1)	2.312(-1)	2.489(1)	-1.546(1)	4.728(-1)
3p65Ax1	2.631(1)	1.648(42)	6.157(-1)	2.579(1)	1.290(42)	6.956(-1)	2.387(1)	-1.576(1)	1.157(0)	2.410(1)	-1.662(1)	1.028(0)
3p65Ax2	2.487(1)	1.661(42)	5.455(-1)	2.455(1)	1.243(42)	5.896(-1)	2.189(1)	-1.539(1)	5.184(-1)	2.231(1)	-1.635(1)	6.811(-1)
3p65Bx2	2.209(1)	2.268(42)	6.983(-1)	2.180(1)	1.739(42)	7.631(-1)	2.022(1)	-1.590(1)	8.292(-1)	2.043(1)	-1.687(1)	1.022(0)
3p65Dx2	1.767(1)	2.770(42)	8.868(-1)	1.755(1)	2.210(42)	9.657(-1)	1.673(1)	-1.651(1)	1.250(0)	1.705(1)	-1.732(1)	1.504(0)
4p64Cx1	3.183(1)	7.623(41)	4.519(-1)	3.123(1)	5.572(41)	5.216(-1)	2.974(1)	-1.444(1)	6.655(-1)	2.931(1)	-1.542(1)	7.126(-1)
4p64Ax1	2.716(1)	1.318(42)	5.351(-1)	2.662(1)	9.871(41)	6.198(-1)	2.410(1)	-1.535(1)	1.051(0)	2.422(1)	-1.625(1)	1.014(0)
4p64Ax2	2.678(1)	1.427(42)	5.885(-1)	2.624(1)	1.034(42)	6.290(-1)	2.311(1)	-1.519(1)	4.769(-1)	2.363(1)	-1.599(1)	6.457(-1)
4p64Bx1	2.292(1)	2.008(42)	6.000(-1)	2.221(1)	1.586(42)	6.911(-1)	2.114(1)	-1.622(1)	1.487(0)	2.103(1)	-1.697(1)	1.296(0)
4p64Bx2	2.285(1)	2.098(42)	6.670(-1)	2.256(1)	1.552(42)	7.109(-1)	2.126(1)	-1.567(1)	7.612(-1)	2.115(1)	-1.661(1)	9.729(-1)
4p64Dx2	1.941(1)	2.707(42)	7.158(-1)	1.916(1)	2.050(42)	7.328(-1)	1.794(1)	-1.610(1)	1.008(0)	1.777(1)	-1.703(1)	1.070(0)
5p11Ax1	3.584(1)	1.590(42)	3.939(-1)	3.506(1)	1.182(42)	4.234(-1)	3.208(1)	-1.524(1)	6.838(-1)	3.256(1)	-1.633(1)	5.941(-1)
5p11Ax2	3.088(1)	1.703(42)	3.719(-1)	3.030(1)	1.253(42)	4.093(-1)	2.679(1)	-1.533(1)	5.063(-1)	2.747(1)	-1.631(1)	4.915(-1)
5p11Bx1	3.143(1)	3.570(42)	4.532(-1)	3.106(1)	2.898(42)	5.148(-1)	2.931(1)	-1.691(1)	1.054(0)	2.916(1)	-1.763(1)	8.763(-1)
5p11Bx2	2.919(1)	3.460(42)	4.310(-1)	2.860(1)	2.666(42)	4.844(-1)	2.474(1)	-1.651(1)	7.994(-1)	2.513(1)	-1.729(1)	7.407(-1)
5p1Gx2	2.020(1)	1.452(42)	7.732(-1)	1.994(1)	1.060(42)	7.960(-1)	1.866(1)	-1.490(1)	7.930(-1)	1.874(1)	-1.604(1)	1.001(0)
6p5Ax1	4.212(1)	1.495(42)	2.262(-1)	4.057(1)	1.079(42)	2.449(-1)	3.634(1)	-1.497(1)	2.554(-1)	3.668(1)	-1.606(1)	3.623(-1)
6p5Ax2	3.539(1)	1.623(42)	2.769(-1)	3.420(1)	1.169(42)	3.041(-1)	3.256(1)	-1.525(1)	4.026(-1)	3.129(1)	-1.609(1)	3.887(-1)
6p5Bx1	3.978(1)	3.934(42)	3.156(-1)	3.901(1)	3.074(42)	3.511(-1)	3.529(1)	-1.674(1)	6.020(-1)	3.581(1)	-1.753(1)	6.281(-1)
6p5Bx2	3.562(1)	3.856(42)	3.186(-1)	3.459(1)	2.916(42)	3.590(-1)	2.940(1)	-1.665(1)	5.378(-1)	2.980(1)	-1.732(1)	5.146(-1)
6p5Gx1	3.041(1)	5.261(42)	4.224(-1)	3.021(1)	4.232(42)	4.686(-1)	2.719(1)	-1.738(1)	8.600(-1)	2.745(1)	-1.801(1)	7.374(-1)
6p5Gx2	2.905(1)	5.212(42)	4.214(-1)	2.848(1)	4.051(42)	4.731(-1)	2.608(1)	-1.711(1)	8.706(-1)	2.570(1)	-1.780(1)	8.509(-1)

Table C2. Same as Table C1, for now for the V, R, and I bands.

Model	V			R			I		
	$t_{\rm rise}$ [d]	Max. [mag]	ΔM_{15} [mag]	$t_{\rm rise}$ [d]	Max. [mag]	ΔM_{15} [mag]	$t_{\rm rise}$ [d]	Max. [mag]	ΔM_{15} [mag]
3p0Cx1	2.472(1)	-1.654(1)	8.496(-1)	2.530(1)	-1.674(1)	7.056(-1)	2.736(1)	-1.680(1)	5.619(-1)
3p0Cx2	2.284(1)	-1.649(1)	8.160(-1)	2.350(1)	-1.678(1)	7.966(-1)	2.500(1)	-1.694(1)	6.794(-1)
3p0Ax1	2.237(1)	-1.709(1)	9.694(-1)	2.297(1)	-1.716(1)	6.774(-1)	2.643(1)	-1.710(1)	4.147(-1)
3p0Ax2	2.189(1)	-1.709(1)	9.159(-1)	2.210(1)	-1.727(1)	7.833(-1)	2.419(1)	-1.729(1)	5.728(-1)
3p0Bx2	1.894(1)	-1.732(1)	1.135(0)	1.903(1)	-1.748(1)	9.340(-1)	2.275(1)	-1.742(1)	7.092(-1)
3p65Cx1	2.731(1)	-1.655(1)	6.946(-1)	2.867(1)	-1.678(1)	6.146(-1)	3.064(1)	-1.694(1)	5.213(-1)
3p65Cx2	2.512(1)	-1.651(1)	5.876(-1)	2.610(1)	-1.680(1)	5.995(-1)	2.801(1)	-1.704(1)	5.346(-1)
3p65Ax1	2.551(1)	-1.723(1)	7.828(-1)	2.668(1)	-1.734(1)	6.099(-1)	2.972(1)	-1.740(1)	3.855(-1)
3p65Ax2	2.384(1)	-1.719(1)	6.861(-1)	2.483(1)	-1.739(1)	6.192(-1)	2.745(1)	-1.755(1)	4.828(-1)
3p65Bx2	2.180(1)	-1.755(1)	9.028(-1)	2.225(1)	-1.771(1)	7.666(-1)	2.484(1)	-1.775(1)	5.134(-1)
3p65Dx2	1.747(1)	-1.781(1)	1.101(0)	1.756(1)	-1.789(1)	9.144(-1)	2.448(1)	-1.777(1)	9.602(-1)
4p64Cx1	3.082(1)	-1.629(1)	5.895(-1)	3.208(1)	-1.653(1)	4.908(-1)	3.335(1)	-1.676(1)	3.852(-1)
4p64Ax1	2.625(1)	-1.692(1)	7.109(-1)	2.830(1)	-1.708(1)	5.696(-1)	3.032(1)	-1.728(1)	3.959(-1)
4p64Ax2	2.545(1)	-1.698(1)	7.175(-1)	2.675(1)	-1.723(1)	6.830(-1)	2.855(1)	-1.745(1)	5.184(-1)
4p64Bx1	2.245(1)	-1.739(1)	7.439(-1)	2.360(1)	-1.744(1)	5.079(-1)	2.621(1)	-1.759(1)	2.354(-1)
4p64Bx2	2.212(1)	-1.743(1)	8.557(-1)	2.288(1)	-1.761(1)	7.248(-1)	2.505(1)	-1.778(1)	4.733(-1)
4p64Dx2	1.889(1)	-1.774(1)	8.477(-1)	1.964(1)	-1.788(1)	7.378(-1)	2.192(1)	-1.803(1)	5.219(-1)
5p11Ax1	3.442(1)	-1.715(1)	4.745(-1)	3.616(1)	-1.734(1)	4.108(-1)	3.920(1)	-1.747(1)	2.772(-1)
5p11Ax2	2.947(1)	-1.722(1)	4.635(-1)	3.111(1)	-1.741(1)	4.293(-1)	3.390(1)	-1.759(1)	2.904(-1)
5p11Bx1	3.097(1)	-1.810(1)	5.142(-1)	3.287(1)	-1.811(1)	4.023(-1)	3.773(1)	-1.814(1)	2.034(-1)
5p11Bx2	2.793(1)	-1.808(1)	5.753(-1)	3.008(1)	-1.818(1)	4.540(-1)	3.518(1)	-1.830(1)	2.501(-1)
5p1Gx2	1.928(1)	-1.711(1)	1.008(0)	1.984(1)	-1.729(1)	8.876(-1)	2.247(1)	-1.739(1)	5.187(-1)
6p5Ax1	3.941(1)	-1.702(1)	2.804(-1)	4.274(1)	-1.731(1)	2.656(-1)	4.564(1)	-1.754(1)	2.064(-1)
6p5Ax2	3.351(1)	-1.707(1)	3.448(-1)	3.529(1)	-1.737(1)	2.999(-1)	3.691(1)	-1.764(1)	2.357(-1)
6p5Bx1	3.863(1)	-1.815(1)	3.708(-1)	4.228(1)	-1.830(1)	3.116(-1)	4.565(1)	-1.849(1)	2.034(-1)
6p5Bx2	3.426(1)	-1.808(1)	4.207(-1)	3.714(1)	-1.831(1)	3.539(-1)	4.026(1)	-1.853(1)	2.563(-1)
6p5Gx1	3.034(1)	-1.853(1)	5.216(-1)	3.259(1)	-1.856(1)	3.841(-1)	3.829(1)	-1.861(1)	2.065(-1)
6p5Gx2	2.813(1)	-1.845(1)	5.403(-1)	3.034(1)	-1.861(1)	4.189(-1)	3.420(1)	-1.878(1)	2.454(-1)

Table C3. Same as Table C1, for now for the J, H, and K bands.

Model	J			H			$K_{\rm s}$		
	$t_{\rm rise}$ [d]	Max. [mag]	ΔM_{15} [mag]	$t_{\rm rise}$ [d]	Max. [mag]	ΔM_{15} [mag]	$t_{\rm rise}$ [d]	Max. [mag]	ΔM_{15} [mag]
3p0Cx1	2.641(1)	-1.675(1)	4.906(-1)	2.806(1)	-1.693(1)	4.347(-1)	2.750(1)	-1.708(1)	4.098(-1)
3p0Cx2	2.284(1)	-1.692(1)	6.945(-1)	2.454(1)	-1.708(1)	6.869(-1)	2.454(1)	-1.729(1)	6.905(-1)
3p0Ax1	2.414(1)	-1.710(1)	4.692(-1)	2.669(1)	-1.722(1)	3.894(-1)	2.669(1)	-1.738(1)	4.142(-1)
3p0Ax2	2.199(1)	-1.730(1)	6.948(-1)	2.338(1)	-1.745(1)	6.082(-1)	2.315(1)	-1.772(1)	6.741(-1)
3p0Bx2	1.884(1)	-1.749(1)	7.121(-1)	2.398(1)	-1.755(1)	9.063(-1)	2.287(1)	-1.791(1)	9.108(-1)
3p65Cx1	3.020(1)	-1.685(1)	4.008(-1)	3.154(1)	-1.708(1)	3.562(-1)	3.050(1)	-1.717(1)	3.897(-1)
3p65Cx2	2.598(1)	-1.696(1)	5.156(-1)	2.731(1)	-1.719(1)	5.484(-1)	2.687(1)	-1.729(1)	5.315(-1)
3p65Ax1	2.751(1)	-1.731(1)	4.328(-1)	3.041(1)	-1.751(1)	2.992(-1)	2.862(1)	-1.764(1)	4.406(-1)
3p65Ax2	2.508(1)	-1.748(1)	4.589(-1)	2.661(1)	-1.766(1)	4.437(-1)	2.610(1)	-1.784(1)	5.417(-1)
3p65Bx2	2.156(1)	-1.778(1)	5.317(-1)	2.289(1)	-1.782(1)	4.064(-1)	2.337(1)	-1.812(1)	5.785(-1)
3p65Dx2	1.680(1)	-1.789(1)	6.537(-1)	2.584(1)	-1.800(1)	1.342(0)	2.460(1)	-1.818(1)	1.322(0)
4p64Cx1	3.424(1)	-1.673(1)	3.000(-1)	3.459(1)	-1.699(1)	2.334(-1)	3.351(1)	-1.701(1)	2.975(-1)
4p64Ax1	2.945(1)	-1.723(1)	4.045(-1)	3.075(1)	-1.749(1)	2.848(-1)	2.902(1)	-1.755(1)	4.206(-1)
4p64Ax2	2.730(1)	-1.744(1)	5.186(-1)	2.855(1)	-1.766(1)	4.412(-1)	2.744(1)	-1.776(1)	5.659(-1)
4p64Bx1	2.394(1)	-1.756(1)	4.317(-1)	2.758(1)	-1.779(1)	3.898(-1)	2.439(1)	-1.787(1)	4.550(-1)
4p64Bx2	2.310(1)	-1.779(1)	6.013(-1)	2.534(1)	-1.798(1)	5.722(-1)	2.398(1)	-1.814(1)	6.702(-1)
4p64Dx2	1.828(1)	-1.801(1)	6.921(-1)	2.262(1)	-1.812(1)	7.200(-1)	2.011(1)	-1.835(1)	7.650(-1)
5p11Ax1	3.786(1)	-1.746(1)	3.279(-1)	3.977(1)	-1.772(1)	2.557(-1)	3.668(1)	-1.768(1)	3.500(-1)
5p11Ax2	3.324(1)	-1.759(1)	3.149(-1)	3.373(1)	-1.788(1)	2.741(-1)	3.241(1)	-1.781(1)	3.361(-1)
5p11Bx1	3.046(1)	-1.803(1)	3.511(-1)	3.766(1)	-1.824(1)	2.917(-1)	3.351(1)	-1.823(1)	3.778(-1)
5p11Bx2	3.080(1)	-1.815(1)	3.231(-1)	3.388(1)	-1.845(1)	3.113(-1)	3.167(1)	-1.839(1)	3.723(-1)
5p1Gx2	2.023(1)	-1.750(1)	6.498(-1)	2.161(1)	-1.761(1)	7.059(-1)	2.023(1)	-1.764(1)	6.957(-1)
6p5Ax1	4.655(1)	-1.752(1)	2.208(-1)	4.769(1)	-1.777(1)	1.514(-1)	4.610(1)	-1.776(1)	2.127(-1)
6p5Ax2	3.882(1)	-1.761(1)	2.103(-1)	3.844(1)	-1.785(1)	1.797(-1)	3.729(1)	-1.789(1)	2.093(-1)
6p5Bx1	4.112(1)	-1.824(1)	2.451(-1)	4.581(1)	-1.850(1)	1.937(-1)	4.249(1)	-1.850(1)	2.555(-1)
6p5Bx2	3.804(1)	-1.836(1)	2.390(-1)	4.205(1)	-1.860(1)	2.350(-1)	3.840(1)	-1.867(1)	2.675(-1)
6p5Gx1	2.877(1)	-1.839(1)	3.291(-1)	3.567(1)	-1.866(1)	3.206(-1)	3.290(1)	-1.865(1)	3.210(-1)
6p5Gx2	2.868(1)	-1.858(1)	2.786(-1)	3.420(1)	-1.881(1)	3.518(-1)	3.125(1)	-1.891(1)	3.571(-1)